

1 **Bedrock ledges, colluvial wedges, and ridgeline water towers:**
2 **Characterizing geomorphic and atmospheric controls on the 2023**
3 **Wrangell landslide to inform landslide assessment in Southeast**
4 **Alaska, USA**

5

6 Joshua J. Roering^{*1}, Margaret M. Darrow², Annette I. Patton³, Aaron Jacobs⁴

7

8 ¹Department of Earth Sciences, University of Oregon, Eugene, OR, USA

9 ²Department of Civil, Geological, and Environmental Engineering, University of Alaska Fairbanks, Fairbanks, AK, USA

10 ³College of Forestry, Oregon State University, Corvallis, OR, USA

11 ⁴National Weather Service, Juneau, AK, USA

12 *Correspondence to:* Joshua J. Roering (jroering@uoregon.edu)

13 **Abstract.** In the past decade, several fatal landslides have impacted Southeast Alaska, highlighting the need to advance our
14 understanding of regional geomorphic and atmospheric controls on triggering events and runout behaviour. A large and long
15 runout landslide on Wrangell Island, with area in the top 0.5% of >14,760 slides mapped in the Tongass National Forest,
16 initiated during an atmospheric river event in November 2023 and travelled >1 km downslope, causing six fatalities. We used
17 field observations, sequential airborne lidar, geotechnical analyses, and climate data to characterize the geomorphic,
18 hydrologic, and atmospheric conditions contributing to the landslide. Rainfall intensities recorded at the Wrangell airport were
19 modest (~1-yr recurrence interval), but rapid snowmelt and drainage from a ridgeline wetland may have contributed to rapid
20 saturation of the landslide. Although strong winds were recorded, we did not observe extensive windthrow, which may
21 downgrade its contribution to slope failure. The landslide mobilized a steep, thick (>4 m) wedge of colluvium that accumulated
22 below a resistant bedrock ledge and entrained additional colluvial deposits as it travelled downslope across cliff-bench
23 topography. The substantial entrainment resulted in an unusually large width, extensive runout, and low depositional slope as
24 the landslide terminated in the coastal environment. Our results suggest that the sequencing of rain- and snow-dominated
25 storms, geologic controls on post-glacial colluvium production and accumulation, and ridgeline hydrology contributed to
26 landslide initiation and mobility. Advances in post-glacial landscape evolution models, frequent lidar acquisition, and
27 additional climate data are needed to inform regional landslide hazard assessment.

28 **1 Introduction**

29 In steep, forested landscapes, shallow landslides serve as the primary agent of erosion (Hovius et al., 1997; Korup et al., 2010;
30 Larsen et al., 2010; Swanson et al., 1987), produce and transport sediment that contributes to aquatic habitat (Geertsema and
31 Pojar, 2007), set the relief structure of mountain ranges (Stock and Dietrich, 2003), and constitute a significant hazard to

32 proximal communities and infrastructure (Godt et al., 2022). In contrast to bedrock landslides whose failures are governed by
33 bedrock properties (Schuster and Highland, 2001; Wyllie and Mah, 2004), shallow landslides composed of loose,
34 unconsolidated material tend to initiate in zones of thick colluvium that experience variable saturation due to precipitation and
35 snowmelt and in turn generate debris flows or debris slides with significant downslope runout and inundation (Gabet and
36 Mudd, 2006; Iverson, 2000). In unglaciated terrain, these shallow landslides often occur in unchannelled valleys (or hollows)
37 at the upstream tips of valley networks that are subject to cycles of infilling and excavation over 10^2 - to 10^4 -yr timescales
38 (Benda and Dunne, 1997; Dietrich et al., 1986; D'Odorico and Fagherazzi, 2003). Characteristic ridge-valley sequences in
39 these settings have facilitated the identification and characterization of shallow landslide and debris flow processes and
40 informed models for soil transport, near-surface hydrologic response, and landslide initiation and runout (Dietrich et al., 1995;
41 Lancaster et al., 2003; Montgomery et al., 1997; Reid et al., 2016; Schmidt et al., 2001).

42 In contrast, in steep, post-glacial settings, terrain morphology tends to be dominated by glacial landforms and deposits such
43 that dissection is patchy and weakly established (Brardinoni and Hassan, 2006). Specifically, shallow landslides tend to initiate
44 within soils of thin-to-moderate thickness (1-3 m) on steep planar slopes and runout to valley floors or low-order channels that
45 are often highly unstable and subject to frequent reorganization (Brardinoni et al., 2009). In these highly dynamic settings,
46 topographic controls on colluvium accumulation along steep, unchannelled slopes is poorly constrained making it difficult to
47 predict landslide entrainment and volumetric growth which largely determine runout and inundation (Brien et al., 2025; Iverson
48 and Ouyang, 2015; Patton et al., 2022). Furthermore, the relative importance of processes that generate the accumulation of
49 colluvium, such as in-situ weathering of till or bedrock, transport of soil or talus deposits, and deposition of allochthonous
50 deposits (e.g., tephra), and thus promote initiation and entrainment is also poorly known (Bovy et al., 2016; Spinola et al.,
51 2024). In these formerly glaciated hillslopes, the lack of a conceptual framework for the production and transport of
52 unconsolidated material inhibits our ability to identify areas susceptible to shallow landsliding, runout, and inundation
53 (Brardinoni et al., 2018; Guthrie, 2002).

54 The triggering of shallow landslides and debris flows in post-glacial terrain is primarily accomplished by storm events that
55 generate intense rainfall over several hours (Fan et al., 2020; Guthrie et al., 2010; Patton et al., 2023; Swanston, 1969) and
56 shallow subsurface stormflow that saturates colluvium and leads to elevated pore pressures. For example, Patton et al. (2023)
57 used logistic regression and Bayesian methods to demonstrate that 3-hr rainfall intensity can effectively differentiate storms
58 that trigger debris flows near Sitka, Alaska. Their analysis forms the basis of the *sitkalandslide.org* warning system that uses
59 National Weather Service (NWS) forecasts to define the 3-hr rainfall intensity with medium (7 mm hr^{-1}) and high (11 mm hr^{-1})
60 levels of risk up to 3 days in the future (Lempert et al., 2023). Additional studies also highlight the importance of rain-on-
61 snow events that can rapidly advect large quantities of water into near surface soil and bedrock and contribute to slope
62 instability (Darrow et al., 2022). Field observations from recently failed head scarps reveal evidence for abundant seepage
63 associated with permeability contrasts along the interface between bedrock, till, or colluvium as well as localized flow

64 associated with fracture networks (Buma and Pawlik, 2021; Swanston, 1970). Notably, the upslope source of shallow
65 groundwater and near-surface runoff that controls hydrologic response in post-glacial steeplands remains unclear owing to the
66 paucity of high-resolution topography, field observations, and instrumental records in these settings. Additional factors
67 contributing to landslide triggering in steep, forested terrain include timber harvest, fire, disease, and infestation, which can
68 affect surface hydraulic properties and root reinforcement that resists sliding (Goetz et al., 2015; Johnson et al., 2000;
69 Swanston, 1969). Extreme wind gusts have also been implicated in landslide initiation (Buma and Johnson, 2015; Lin et al.,
70 2025; Parra et al., 2021) although the relative importance is difficult to determine and the mechanism by which wind gusts
71 may contribute to slope failure is unclear and may include physical disturbance, progressive root failure, directed rainfall, or
72 opening of hydrological pathways (Guthrie et al., 2010; Rulli et al., 2007). High winds can also contribute to rapid snowmelt
73 (Hasebe and Kumekawa, 1995) and warm atmospheric rivers have been shown to promote snowmelt that substantially
74 increases stream discharge (Guan et al., 2016; Hatchett, 2018; Henn et al., 2020).

Formatted: Font: Not Bold

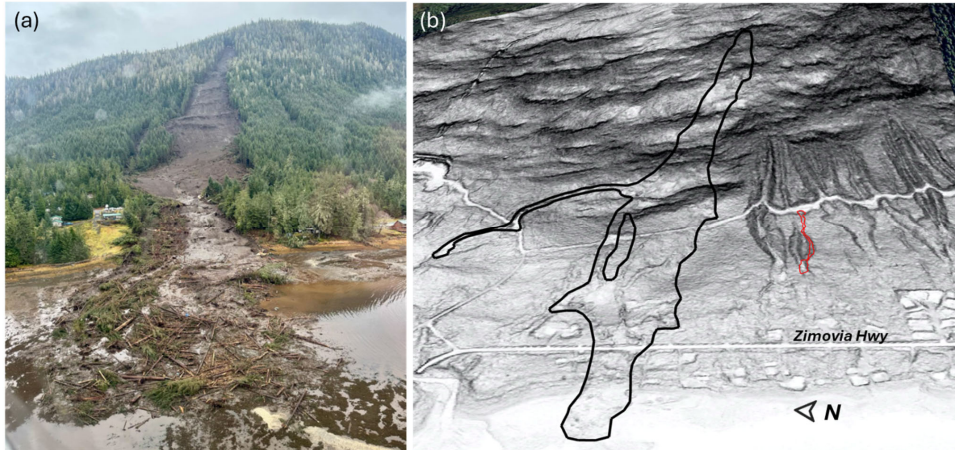
Formatted: Font: Not Bold

75 The runout and inundation of landslides in post-glacial settings tends to be highly variable owing to variations in landscape
76 dissection and the availability of unconsolidated material for entrainment. Most generally, the weakly-dissected slopes tend to
77 generate fewer mobile slides that deposit on steeper slopes compared to slides in unglaciated settings (Booth et al., 2023;
78 Vascik et al., 2021). Forest cover also affects landslide mobility, and the dense forest cover and large woody debris
79 characteristic of many post-glacial settings favour lower mobility landslides (Booth et al., 2020). An abundance of datasets
80 and models for the production and redistribution of colluvium that contribute to debris flow entrainment and volumetric growth
81 have been generated in unglaciated settings (DiBiase et al., 2017; Gorr et al., 2022; Guilinger et al., 2023; Lamb et al., 2011;
82 Reid et al., 2016; Rengers et al., 2020), but we lack both a framework and datasets that enable us to predict the runout, volume,
83 and inundation of debris flows in post-glacial settings.

84 The need to improve our understanding of post-glacial shallow landslide triggers and processes in SE Alaska was highlighted
85 by a large, catastrophic landslide that occurred on Wrangell Island on the evening of November 20, 2023. The landslide
86 initiated during an intense rainfall event and entrained large quantities of colluvium and trees as it travelled downslope (Fig.1).
87 Before terminating in Zimovia Strait, the landslide travelled over 1 km, inundated Zimovia Highway, destroyed three homes,
88 and caused six fatalities (Nicolazzo et al., 2024), making it one of the deadliest landslides in Alaska history. This event was
89 preceded and followed by several other fatal landslides in the region, including the 2015 Sitka, 2020 Haines, and 2024
90 Ketchikan events. This concentration of activity motivates a detailed assessment of the geomorphic, geologic, and atmospheric
91 factors contributing to the initiation and runout of impactful landslides in SE Alaska. Here, we use an array of tools to
92 characterize the 2023 Wrangell landslide and describe how these findings will advance our ability to assess landslides in the
93 region. In particular, our analysis addresses: 1) atmospheric processes, including precipitation and wind, that contributed to
94 event triggering, 2) controls on the accumulation of unconsolidated material that promotes landslide initiation, downslope
95 entrainment, and volumetric growth, 3) geologic and topographic controls on landslide runout and inundation, and 4) controls

96 on the organization and evolution of upslope drainage networks that modulate hydrologic response at the initiation zone. We
97 leverage field observations, geotechnical measurements, sample analyses, climate data, change detection analysis from
98 sequential airborne lidar data, an existing US Forest Service landslide inventory, and hydrologic flow routing analyses to assess
99 the 2023 Wrangell landslide. Our findings provide critical information for identifying landslide triggers, mapping susceptible
100 initiation zones, and modelling runout and inundation, and we propose specific ~~steps~~ steps, and research needs to advance
101 landslide assessment in SE Alaska and other post-glacial landscapes to help reduce risk and minimize exposure during future
102 events.

103



104 **Figure 1.** The November 20, 2023 MP11.2 Wrangell landslide: (a) Oblique aerial photograph facing east taken on November 22, 2023 by
105 B. Salisbury (DGGS), and (b) oblique lidar slopeshade image.

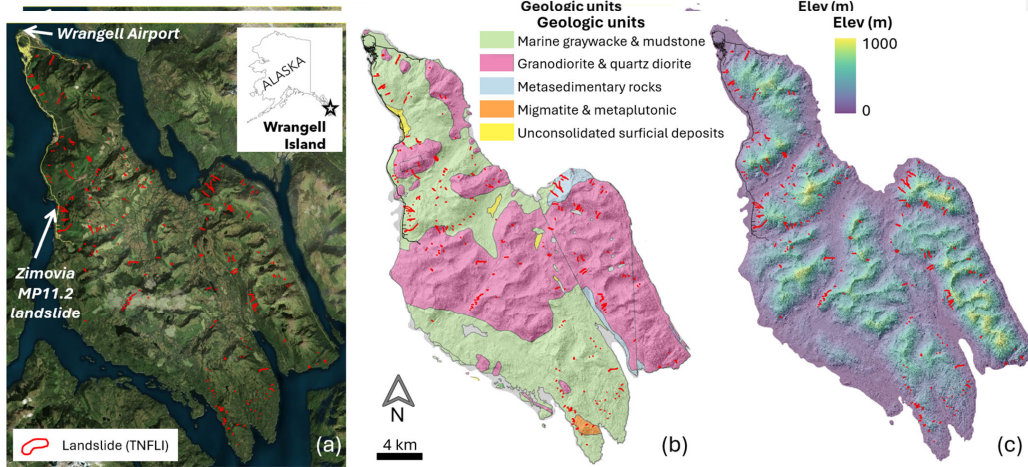
106 2 Study site

107 2.1 Geology and geomorphology

108 Situated in the southern half of southeast (SE) Alaska, Wrangell Island (Fig. 2) is composed of an assemblage of marine rocks
109 in the Gravina coastal belt on the eastern margin of the Alexander Terrane that composes a substantial fraction of the region
110 (Fig. 2b) (Haeussler, 1992; Wheeler and McFeely, 1991). Bedrock of the northern half of the island includes Cretaceous and
111 Jurassic graywacke and Cretaceous intrusions (Karl et al., 1999). These turbidites and igneous rocks were deformed in the
112 Late Cretaceous during the closing of a marine sedimentary basin between the Alexander terrane to the west and the Stikine
113 terrane to the east (Haeussler, 1992). The graywacke is part of the Seymour Canal Formation, a unit with fine-grained,

114 rhythmically bedded turbidite deposits that are regionally recrystallized to slate or phyllite. The sandstone layers tend to be
115 highly resistant and often form bedrock cliffs in areas with favorable dip direction.

116



117 **Figure 2.** Maps of Wrangell Island overlain with 256 landslide polygons (red) from the Tongass National Forest Landslide
118 Inventory (TNFLI): (a) satellite imagery from Bing Satellite layer in QGIS Quick Map Services plug-in, (b) geologic units,
119 and (c) lidar elevation and hillshade image.

120 The SE Alaska archipelago, including Wrangell Island, has been repeatedly glaciated, most recently during the Last Glacial
121 Maximum, generating characteristic landforms, including cirques, uplifted shorelines, and broad U-shaped valleys (Fig. 2c)
122 (Hamilton, 1994; Mann and Hamilton, 1995). By 13 to 15 kya, the margins of the Cordilleran Ice Sheet had retreated from SE
123 Alaska fjords, channels, and interior passages, leaving isolated or stranded ice caps on some islands, with alpine or tidewater
124 glaciers in many valleys and mountain peaks protruding above alpine glaciers (Carrara et al., 2003; Menounos et al., 2017).
125 Broad and gentle uplifted shorelines (sometimes more than 100 m above sea level) with beach ridges, storm berms, and weak
126 dissection, are abundant along coastlines in portions of SE Alaska (Baichtal et al., 2021) and may influence landslide runout.

127 On hillslopes, post-glacial landscape evolution is highly variable and some areas, particularly portions of western Wrangell
128 Island, experience widespread slope modification from rockfall, talus accumulation, localized gullying, and landsliding.

129 **2.2 Climate and vegetation**

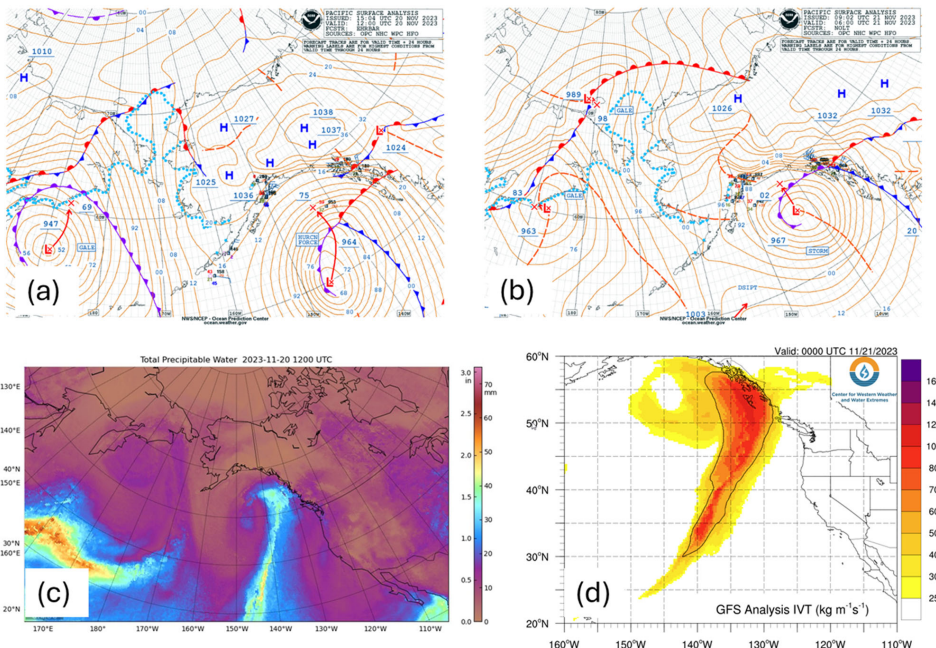
130 SE Alaska is a regional temperate rain forest with a maritime climate (Wendler et al., 2016). In Wrangell the mean annual
131 precipitation is roughly 2 m, most of which falls as rain at low elevation with the proportion of rain-to-snow decreasing with
132 elevation. In Wrangell and across SE Alaska, nearly all high-intensity rainstorms are associated with atmospheric rivers (ARs)
133 (Nash et al., 2024), which are long (>2000 km), narrow (<500 km), moisture-laden currents in the lower troposphere (Neiman
134 et al., 2008; Ralph et al., 2004). When ARs, which are most active August to November in SE Alaska, make landfall, orographic
135 forcing can result in higher precipitation in mid-slope locations and on slope aspects that coincide with the trajectory of
136 incoming ARs (Marra et al., 2022; Rulli et al., 2007). Although ARs account for only ~33% of annual precipitation, they
137 generate 90% of extreme precipitation in the region (Sharma and Déry, 2020). As a result, ARs trigger the vast majority of
138 shallow landslides along the Pacific coast of North America and SE Alaska (Cordeira et al., 2019; Oakley et al., 2018)
139 Much of SE Alaska is densely forested with mixed conifer forests of western hemlock (*Tsuga heterophylla*), Sitka spruce
140 (*Picea sitchensis*), western red cedar (*Thuja plicata*), yellow cedar (*Callitropsis nootkatensis*), and mountain hemlock (*Tsuga*
141 *mertensiana*) (Harris and Farr, 1974; Hees and Mead, 2005). Disturbed and riparian areas host locally abundant red alder and
142 black cottonwood. Non-forested regions include high-elevation tundra vegetation and emergent wetlands (e.g., muskeg),
143 surface water, glaciers, and snow/icefields (Flagstad et al., 2018). On Wrangell Island, logging since the 1950's along lower
144 elevations has resulted in a mosaic of forest stand age. Although recent hemlock sawfly and western blackheaded budworm
145 outbreaks have resulted in swaths of mid-elevation trees that have dropped their needles (Howe et al., 2024), the extent of tree
146 mortality and impact on root systems, and thus slope stability, is not yet established.

147 **2.3 Landslides in Southeast Alaska**

148 Based on the Tongass National Forest Landslide Inventory (TNFLI), which includes >20,000 mapped slope failures and slide-
149 prone areas (U.S. Forest Service, 2025b), the vast majority (>80%) of landslides in SE Alaska are debris flows or unchannelized
150 debris avalanches that initiate within weathered till or colluvium during periods of intense rainfall (Fig 2a). The recent fatal
151 landslides in SE Alaska were colluvial landslides, except for the 2020 Beach Road landslide in Haines that initiated within
152 shallow bedrock during the December 2020 rain-on-snow event (Darrow et al., 2022). Extensive field-based research on
153 landslide processes, particularly root reinforcement and hydrologic response, originated in the 1960s on Prince of Wales Island
154 following increased landslide activity after timber harvest (Johnson et al., 2000; Swanston, 1969, 1970, 1973). These studies
155 indicated that tree mortality affected landslide density as well as runout, such that landslides in harvested areas exhibited higher
156 mobility (Booth et al., 2020; Buma and Johnson, 2015). The wide glacial valleys and weakly-dissected slopes in SE Alaska
157 tend to favour infrequent landslide delivery to streams and most debris flow deposits contribute to fans or footslope deposits.

158 **2.4 The November 20, 2023 atmospheric river and impacts on Wrangell Island**

159 A hurricane-force 964 mb low pressure system lifted out of the North Pacific into the Gulf of Alaska during the early morning
 160 hours of November 20, 2023 (Figure 3a). This low-pressure system proceeded along a north-northwest track, with the warm
 161 front moving over southern and central SE Alaska before the front pushed north through the evening hours (Fig. 3b). A cold
 162 air mass over northern SE Alaska and the Yukon produced a zone of high pressure and a strong pressure gradient across SE
 163 Alaska. This colder air likely produced ~~some~~ snowfall at higher elevations prior to the arrival of warm, moist air. This weather
 164 system included significant subtropical moisture and additional AR characteristics evident in satellite imagery (Fig. 3c). At 3
 165 PM on November 20, the CIMMS Model analysis of Integrated Water Vapor Transport (IVT), a commonly used indicator of
 166 ARs, indicated very high IVT over the southern half of SE Alaska (Fig. 3d).



167 **Figure 3.** The November 20, 2023 atmospheric river event: (a) NOAA surface analysis from imagery from November 20 at
 168 4am Alaska Standard Time, (b) NOAA surface analysis from imagery from November 20 at 10pm Alaska Standard Time, (c)
 169 Total Precipitable Water from the Cooperative Institute for Meteorological Satellite Studies (CIMSS) Morphed Integrated

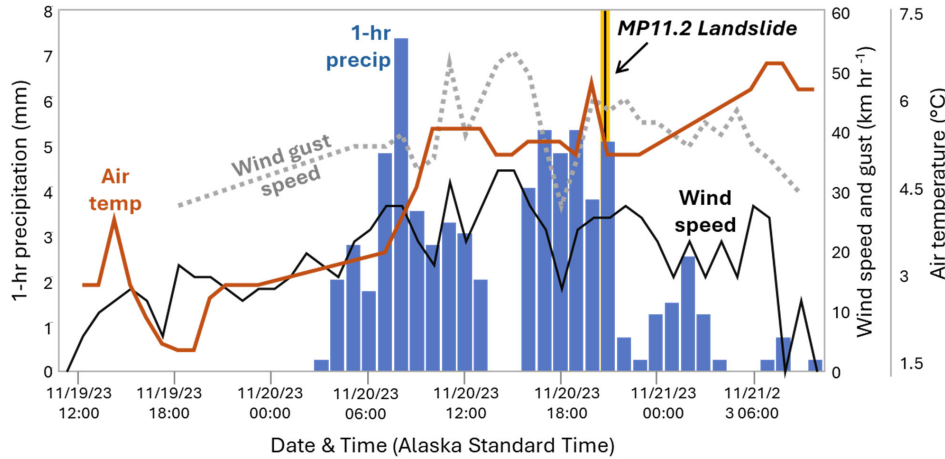
170 Microwave Total Precipitable Water (MIMIC-TPW) for November 20 at 4am Alaska Standard Time, (d) Integrated Water
171 Vapor Transport (IVT) from Center for Western Weather and Water Extremes (C3WE) from November 20 at 4pm.

172

173 Heavy precipitation and high wind gusts began in the morning hours of November 20 and warm air and moisture combined
174 with high winds likely melted snow at higher elevations. That afternoon, numerous landslides and road blockages were reported
175 on Prince of Wales Island near Craig, Klawock, and Black Bear. The front shifted to an eastward trajectory in the early evening
176 hours, as heavy rain and winds shifted towards Wrangell Island, and reports of the Zimovia Highway milepoint-point
177 (MP)(MP) 11.2 landslide were received just before 9 pm Alaska Standard Time. The front continued eastward, and rain and
178 winds diminished through the night. The 24-hr precipitation totals on Prince of Wales varied from <5 cm to >16 cm on the
179 east and west sides of the island, respectively (National Oceanographic and Atmospheric Administration (NOAA), 2024). At
180 Wrangell airport, which is situated at sea level near the northern tip of the island and over 15 km north of the MP11.2 landslide
181 (Fig. 2a), 8 cm of rainfall was recorded in 24 hours, and nearly half of that rainfall total was delivered steadily between 3 pm
182 and 9 pm (Fig. 4). Peak wind speed and gusts of 30 and 50 km hr⁻¹, respectively, occurred from 11 am to 3 pm and sustained
183 at high levels through the evening. Air temperature rose rapidly in the morning and remained above 5°C. A remote weather
184 station located ~25 km west of the MP11.2 slide at 275m above sea level on Zarembo Island recorded similar wind speeds as
185 the Wrangell airport but notably logged a short period of gusts >100 km hr⁻¹ around 7 pm in conjunction with a southward
186 shift in direction of the front (Nicolazzo et al., 2024). Local observations during the day of the storm are notable because
187 several residents reported: 1) rainfall to be more intense along Zimovia Highway than in Wrangell, and 2) significant snow
188 cover at mid-to-high elevations prior to the November 20 storm that melted by November 21.

Formatted: Superscript

Formatted: Superscript



189 **Figure 4.** Time series of hourly climate data from Wrangell Airport spanning November 19 to 21, 2023, including: 1-hr
 190 precipitation (blue bars), average wind speed and maximum wind gusts (black and dashed grey lines, respectively), and air
 191 temperature (red line). The MP11.2 landslide occurred at ~9pm on November 20 (vertical yellow/black line).

192
 193 On November 21, Alaska Governor Dunleavy issued a state disaster declaration, and the Alaska Division of Geological &
 194 Geophysical Surveys (DGGS) was contracted to document landslides triggered on Wrangell Island during the storm. DGGS
 195 used airborne lidar acquired in July and on November 28-29, 2023, to estimate the character and volume of the MP11.2 and
 196 nearby landslides (Nicolazzo et al., 2024). For the MP11.2 landslide, they noted under 80,000 m³ of erosion, thick soil
 197 entrained along bedrock benches, and an abundance of soil and large woody debris (with a negligible amount of bedrock)
 198 composing the deposit. Portions of the deposit had been removed before the post-event lidar acquisition and the deposit
 199 travelled nearly 150 m into the ocean, such that a small but non-negligible fraction of the deposit was not captured with lidar
 200 differencing.

201 **3 Methods**

202 **3.1 Overview**

203 To assess and quantify controls on the initiation and runout of the MP11.2 landslide, we performed a wide array of analyses
 204 and generated observations from fieldwork, community events, airborne lidar, hydrologic modelling, weather data, and

205 geotechnical testing. We endeavoured to address community-generated queries, such as the potential role of wind as a
206 triggering agent and mechanisms responsible for the anomalously large size of the landslide.

207 **3.2 Landslide geometry**

208 To contextualize the MP11.2 landslide, we analysed the landslides previously mapped on Wrangell Island included in the
209 TNFLI (n=20,235) (U.S. Forest Service, 2025b). We excluded snow avalanche chutes, snow avalanche fields, and debris
210 avalanche fields because these extensive features reflect landforms that accumulate over time rather than discrete landslide
211 events. For the remaining landslides (n=14,670), we identified those occurring on Wrangell Island and quantified the area,
212 mobility (defined as H/L, where H is elevation difference between the head scarp and deposit and L is landslide length, defined
213 as the horizontal distance between the head scarp and deposit), and aspect ratio (defined as W/L, where W is average landslide
214 width).

215 **3.3 Field observations, sampling, and analyses**

216 To document failure mechanisms and runout behaviour, we traversed the entire length of the landslide, observing evidence of
217 entrainment and deposition, and mapping localized seepage in the head scarp area. We collected representative soil samples,
218 from which we determined gravimetric water content (American Society for Testing Materials, 2017a); particle-size
219 distribution, consisting of sieve analysis (American Society for Testing Materials, 2017b), sedimentation analysis (American
220 Society for Testing Materials, 2021), and specific gravity testing (American Society for Testing Materials, 2014b); Atterberg
221 limits (American Society for Testing Materials, 2017a), and organic content by loss on ignition (Alaska Department of
222 Transportation and Public Facilities, 2023). We also collected two volumetric samples using a soil sampler with inner brass
223 rings, from which we determined dry unit weight and volumetric water content. We classified samples using the Unified Soil
224 Classification System (American Society for Testing Materials, 2017a). We also collected estimates of intact bedrock strength
225 using two Rock Schmidt Rebound Hammers (N-type and L-type, with impact energies of 2.207 Nm and 0.735 Nm,
226 respectively). We followed standard methods (American Society for Testing Materials, 2014a) with the exception that we did
227 not use a grinding stone on the in-situ rock faces. We also collected slices (or “cookies”) of four trees entrained in the deposit
228 to determine their ages and obtained 35 bedrock and/or joint surface orientation measurements for kinematic analysis. Finally,
229 we ventured onto the ridgeline above the landslide to document the upslope accumulation area that contributes surface water
230 flow to the head scarp region.

231 **3.4 Topographic analysis: change detection, morphology, and hydrologic modelling**

232 To quantify the pattern of erosion and deposition, and controls on colluvial deposits and their entrainment in the landslide, we
233 used the July 2023 and November 2023 lidar for change detection and topographic analysis (Zechmann et al., 2023, 2024).
234 Both datasets have 0.5-m pixel spacing, high bare earth point density (>5 pts m⁻²), and high accuracy (<10 cm error in bare
235 and vegetated areas). We used QGIS for our analyses and mapped the landslide extent using high-resolution imagery acquired

236 by the Alaska Department of Transportation and Public Facilities (ADOT&PF) and the airborne lidar data. By comparing
237 numerous stable features in both lidar datasets we determined systematic offset to be negligible (<3 cm). For change detection,
238 we applied raster-based subtractions and created a point layer for the landslide pixels, which we attributed with slope, elevation,
239 land surface change using the digital terrain model (DTM, i.e., bare earth data), and vegetation change using the digital surface
240 model (DSM, i.e., first return data). We used the derived points and their attributes in three primary ways: 1) maps of DTM
241 and DSM change across the landslide and surrounding terrain, 2) plots of swath (10-m wide) averaged profiles of elevation,
242 slope, and DTM / DSM change along a longitudinal transect that spans the central axis of the primary landslide, and 3)
243 construction of a comprehensive mass balance of DTM change (i.e., erosion and deposition) along a cross-sectional transect
244 that spans the entire width of the landslide.

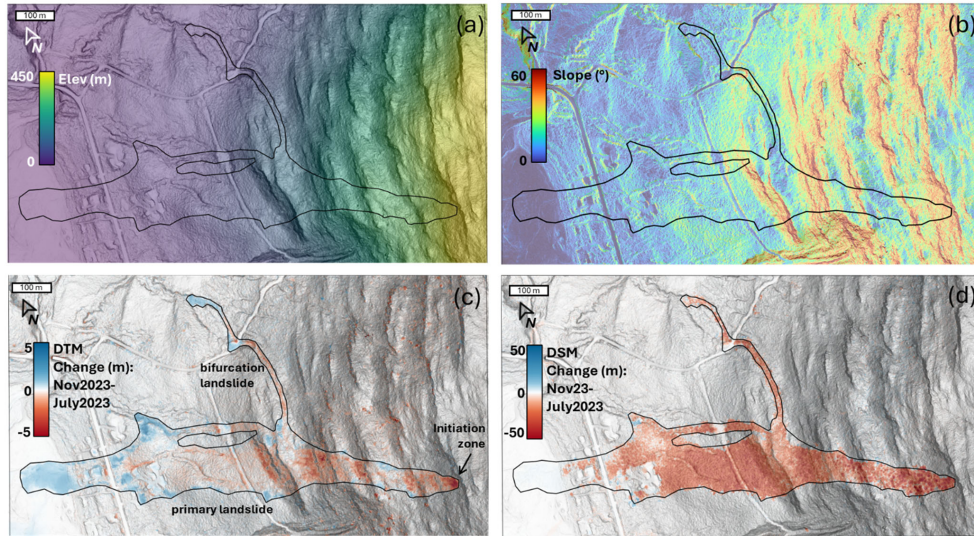
245 For the hydrologic modelling, we used TopoToolbox to define flow paths above the landslide scarp by removing sinks and
246 defining flow directions and flow accumulation using a multiple flow direction (MFD) algorithm that partitions flow to all
247 downslope pixels in proportion to the gradient of each pixel (Schwanghart and Scherler, 2014). In addition, we accessed the
248 U.S. National Wetlands Inventory (Flagstad et al., 2018) in conjunction with our flow model to assess the potential contribution
249 of wetlands to surface water flow and landslide triggering.

250 4 Results

251 4.1 Landslide geometry

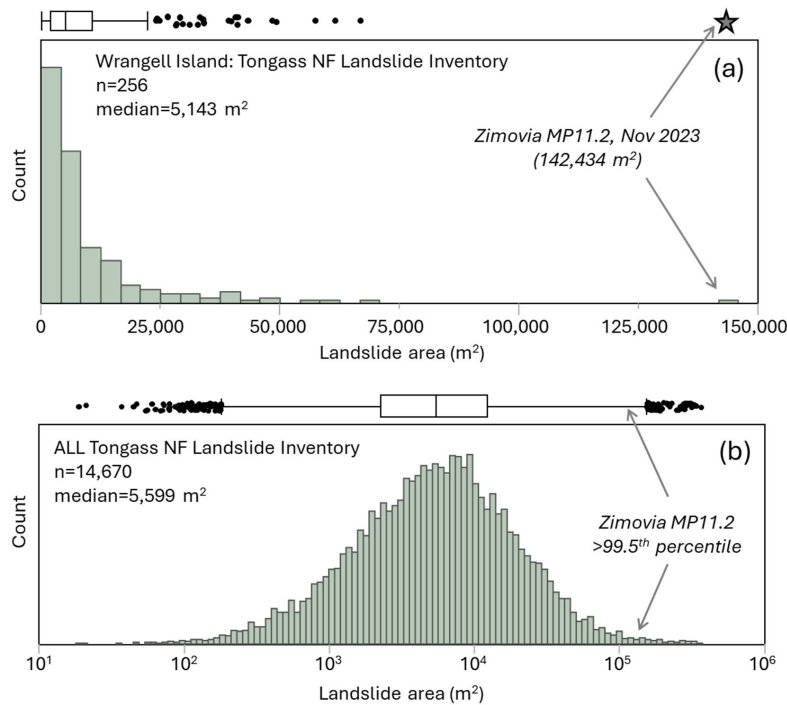
252 The MP11.2 landslide has an area greater than 142,000 m² and initiated at 454m above sea level before flowing downslope
253 >1km and depositing into the coastal marine environment (Fig. 5a). Although the width of the landslide averages 130 m, it is
254 widest in the middle of the runout zone, and relatively narrow (<50m) at the initiation zone and terminus. Our analysis of
255 landslides on Wrangell Island and in the TNFLI demonstrates that the MP11.2 landslide is notable for its areal extent (Fig.
256 6a), which is more than twice the size of the next largest Wrangell Island landslide. When compared to the entire TNFLI, the
257 MP11.2 landslide has a larger area than 99.5% of the landslides (Fig. 6b), which further demonstrates its exceptional size.
258 Given that landslide mobility (quantified as H/L, the value of which decreases with increased mobility) tends to vary with
259 landslide size (Iverson et al., 2015; Rickenmann, 1999), we plotted H/L versus landslide area for the Wrangell Island landslides
260 and fitted a logarithmic trend, such that H/L decreases slightly with area (Fig. 7a). In this context, the MP11.2 landslide is
261 situated on the trend and thus does not appear notable for its mobility relative to its area. Because the MP11.2 landslide is
262 maintained a relatively wide footprint along most of its path, we also plotted W/L versus area (Fig. 7b) and noted a robust
263 power-law trend indicating that slides tend to become increasingly elongate as they get bigger. In this context, the MP11.2
264 landslide is anomalous for its large W/L value relative to its area. Specifically, the landslide plots well above the trend and
265 only one of the 25 next largest landslides has a similar positive deviation above the area-W/L curve (Fig. 7b). In summary, the
266 landslide did not appear to exhibit uncommon mobility as defined by H/L values, but rather it attained a large area while also
267 maintaining substantial width, which contributed to its extensive inundation area and devastating impact.

Formatted: Superscript

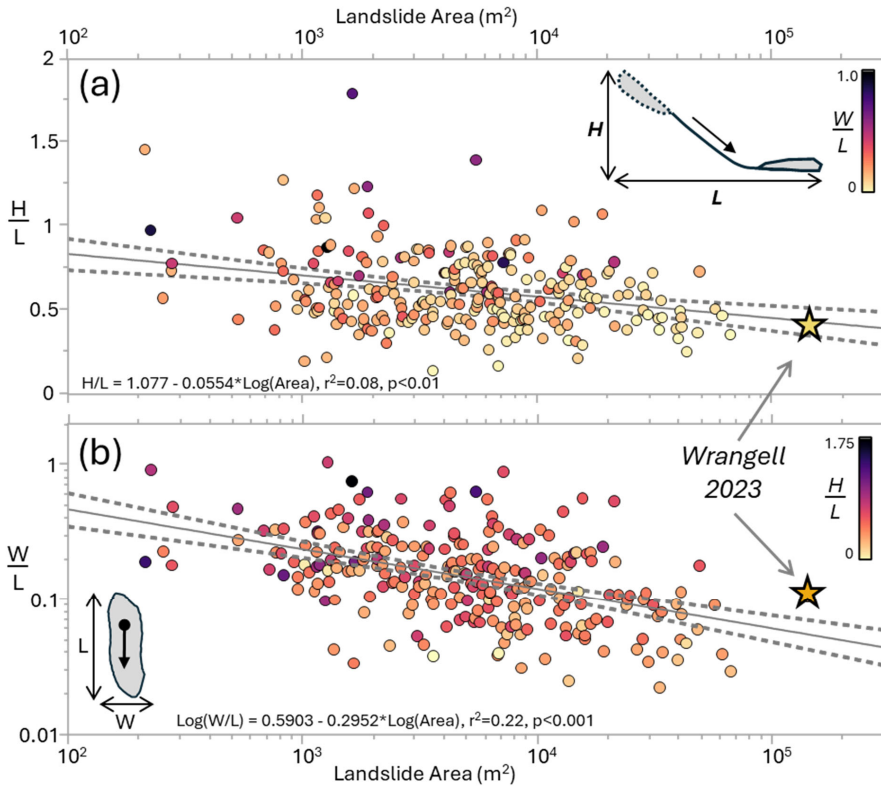


269 **Figure 5.** Lidar-derived maps of the MP11.2 landslide: (a) elevation above sea level in meters, (b) slope in degrees, (c)
270 DTM change (land surface or bare earth), and (d) DSM change (first return or canopy) with November 2023 dataset subtracted from
271 the July 2023 dataset such that negative values (red) reflect decreases and positive values (blue) reflect increases.

272
273



274 **Figure 6.** Histograms of landslide area from the TNFLI for (a) Wrangell Island and (b) all of the TNFLI, note the log scale.
 275 The box-whisker plots above each histogram convey the median, interquartile range and outliers and the star denotes the
 276 MP11.2 landslide.

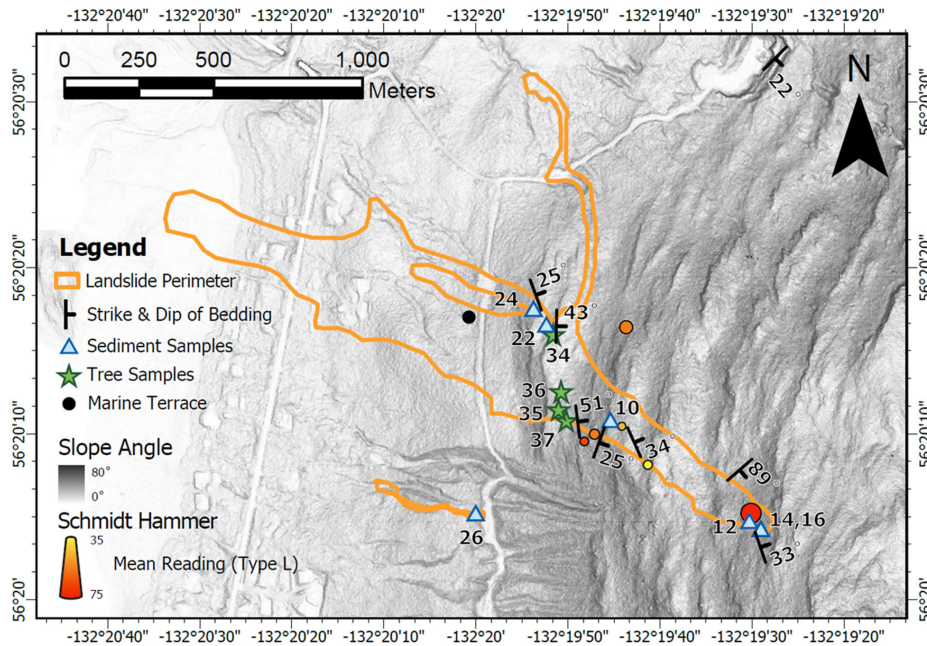


277 **Figure 7.** Plots of landslide characteristics for Wrangell landslides in the TNFLI. (a) Variation of mobility (H/L) with area,
278 and (b) variation of landslide aspect ratio with area. Note that the star indicates the MP 11.2 landslide in a and b. The solid
279 black and dashed grey lines denote the regression fits and 95% confidence intervals for the equations indicated in a and b.
280 Individual points are coloured by W/L in a and H/L in b.

281 **4.2 Geologic units, bedrock structure, and soil properties**

282 Marine sedimentary rocks of the Seymour Canal Formation (Karl et al., 1999) are exposed in the landslide and a bedrock
283 quarry approximately 1.5 km north of the landslide head scarp (NE corner of map in Fig. 8). Bedrock lithology includes
284 interbedded shale and graywacke typical of turbidite sequences with bedding dipping into the hillslope (to the east) within the
285 landslide (Fig. 8). Local metasedimentary rocks on nearby hillslopes (slate and minor phyllite) indicate low-grade

286 metamorphism in the study area. Graywacke beds are 0.25- to 5-m thick as observed in the field and form benchlike
 287 topography, with the resistant graywacke creating subvertical cliff bands within the landslide margin and across undisturbed
 288 hillslopes, and the relatively weak shale forming low-gradient slopes (Fig. 5b). Bedding orientation in the quarry dips to the
 289 southeast, indicating hillslope-scale folding (Fig. 8). In addition to bedding geometry, we documented three joint sets to assess
 290 the potential for rock slope instability along the resistant bedrock cliffs. Preliminary kinematic analysis of discontinuities using
 291 conservative friction angle estimates of 15° and 30° for shale and sandstone, respectively (Gonzalez de Vallejo and Ferrer,
 292 2011), indicates that flexural toppling is possible while other rock failure mechanisms (direct toppling, wedge and planar
 293 failure) are unlikely (supplemental materials).



294
 295 **Figure 8.** Lidar hillshade map of MP11.2 landslide showing locations of field measurements and samples acquired during the
 296 August 2024 field campaign. Strike and dip and Schmidt Hammer values denote averages within each sample locale.
 297
 298 We collected a total of 60 readings with each of the Schmidt Hammers. Using a correlation for sandstone, siltstone, and
 299 mudstone that does not require rock density and uses the L-type hammer (Aydin and Basu, 2005), our estimates of uniaxial

300 compressive strength (UCS) average 90 MPa for measurements taken outside the lateral margins of the landslide body, 82
301 MPa for measurements in the middle of the landslide body, and 148 MPa for measurements taken on massive greywacke
302 exposed in the head scarp (supplemental materials). These values are typical for graywacke (Gonzalez de Vallejo and Ferrer,
303 2011) and indicate that the estimated UCS of the exposed graywacke in the head scarp is 80% higher than that within the lower
304 landslide body and 64% higher than bedrock exposures adjacent to the MP11.2 landslide.

305 In exposures along the landslide flanks, we observed colluvium as discontinuous “wedges” at the base of bedrock cliffs,
306 including a ~4 m thick deposit that constitutes the initiation zone (Fig. 9a). The matrix of the colluvium was brown, organic
307 silty sand to silty sand with gravel (SM), similar to displaced landslide material observed downslope. The material properties
308 of the colluvium imply moderate frictional strength, minimal weathering or alteration, and relatively high permeability. All of
309 the samples tested were non-plastic (supplementary materials). In an area scoured by the landslide in its depositional zone, we
310 also observed a deposit of sand and subrounded, imbricated gravel characteristic of coastal marine sediments. The deposit is
311 exposed just below the USFS road at approximately 100 m elevation, which is consistent with estimated glacial isostatic
312 adjustment documented for the region (Baichtal et al., 2021).

313



314 **Figure 9.** Photographs of key features identified in the field: (a) view to the north across the head scarp, exposing thick (~4m)
 315 colluvial wedge in lateral margin, (b) ridgeline wetland or muskeg that drains to the head scarp, and (c) oblique view of mid-
 316 slope location (~1,000 m on transect; see Fig. 11) depicting high relief and resistant cliff-forming unit and patch of live
 317 blueberry bushes just below the top of the bedrock cliff. Note person for scale.

318 4.3 Landslide initiation and triggering factors

319 The initiation zone for the MP11.2 landslide has an average slope of $42\pm2.5^\circ$ and is approximately 30-m wide and 26-m long
 320 (Fig. 5b, d). According to lidar differencing of the pre- and post-event DTMs, the average thickness of the initiation zone is
 321 4.5 ± 0.7 m (Fig. 5c), which is thick relative to many landslides observed in the Tongass National Forest. In the days following
 322 the landslide, aerial imagery acquired by the Alaska Department of Transportation and Public Facilities (ADOT&PF) revealed
 323 prodigious seepage emanating from the SE corner of the head scarp, and during our August 2024 field campaign we noted
 324 localized seepage in that location despite negligible rainfall in the preceding days. Additional triggering factors include

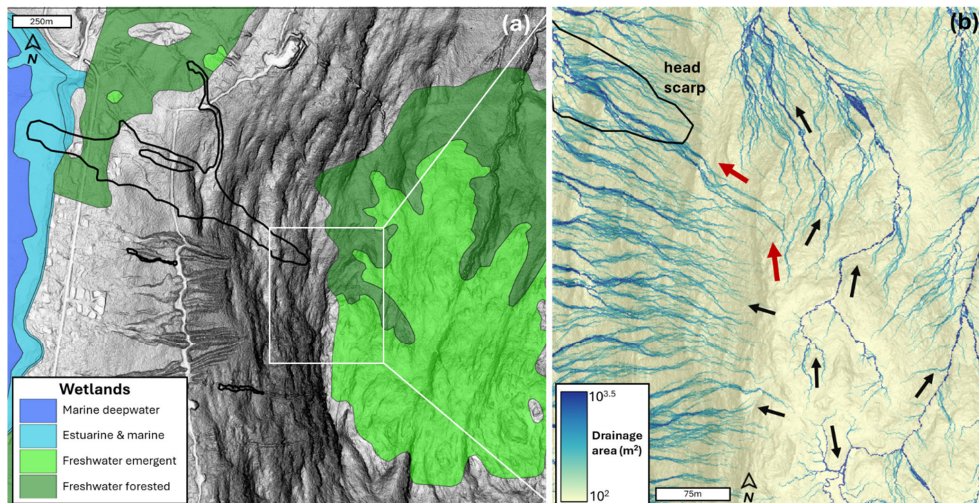
325 compromised root reinforcement, and we noted an abundance of standing Western hemlock trees without needles just beyond
326 the northern and southern margins of the initiation zone.

327 In the 6 hours prior to the MP11.2 landslide, rainfall intensity at the airport averaged 5 mm hr^{-1} (Fig. 4), which corresponds to
328 a ~ 1 -yr return interval (National Oceanographic and Atmospheric Administration (NOAA), 2024). In addition, the maximum
329 3-hr intensity just prior to the slope failure was less than the 7 mm hr^{-1} intensity threshold that delineates an elevated level of
330 risk in the Sitka region. Notably, high winds and warm temperatures characterized the 12-hour period prior to the landslide,
331 and these changes may have contributed to the failure through mechanical disturbance and rapid delivery of snowmelt to the
332 initiation zone, ~~respectively~~. Observational records of these potential triggering factors proximal to the landslide are lacking,
333 so we explored alternative sources of evidence. To assess the potential role of wind disturbance in landslide triggering we used
334 differencing of the canopy (or DSM) lidar data to map wind throw (or tree turnover) as a signature of canopy disturbance
335 proximal to the initiation zone (Fig. 5d). Consistent with our field observations, our map of DSM change does not reveal
336 evidence for widespread canopy disturbance beyond the margins of the landslide. In fact, the DSM change map revealed less
337 than 10 individual and localized tree turnover events dispersed within several kilometres of the MP11.2 landslide.

338

Formatted: Superscript

Formatted: Superscript



339 **Figure 10.** Lidar maps of MP11.2 landslide and relevant drainage features. (a) Shaded relief image of landslide and extent of
340 ridgeline wetland from the National Wetlands Inventory, (b) map of contributing drainage area along the ridgeline above the
341 MP11.2 landslide. Note the radial flow pattern that includes a significant area flowing to the head scarp (red arrows).

342

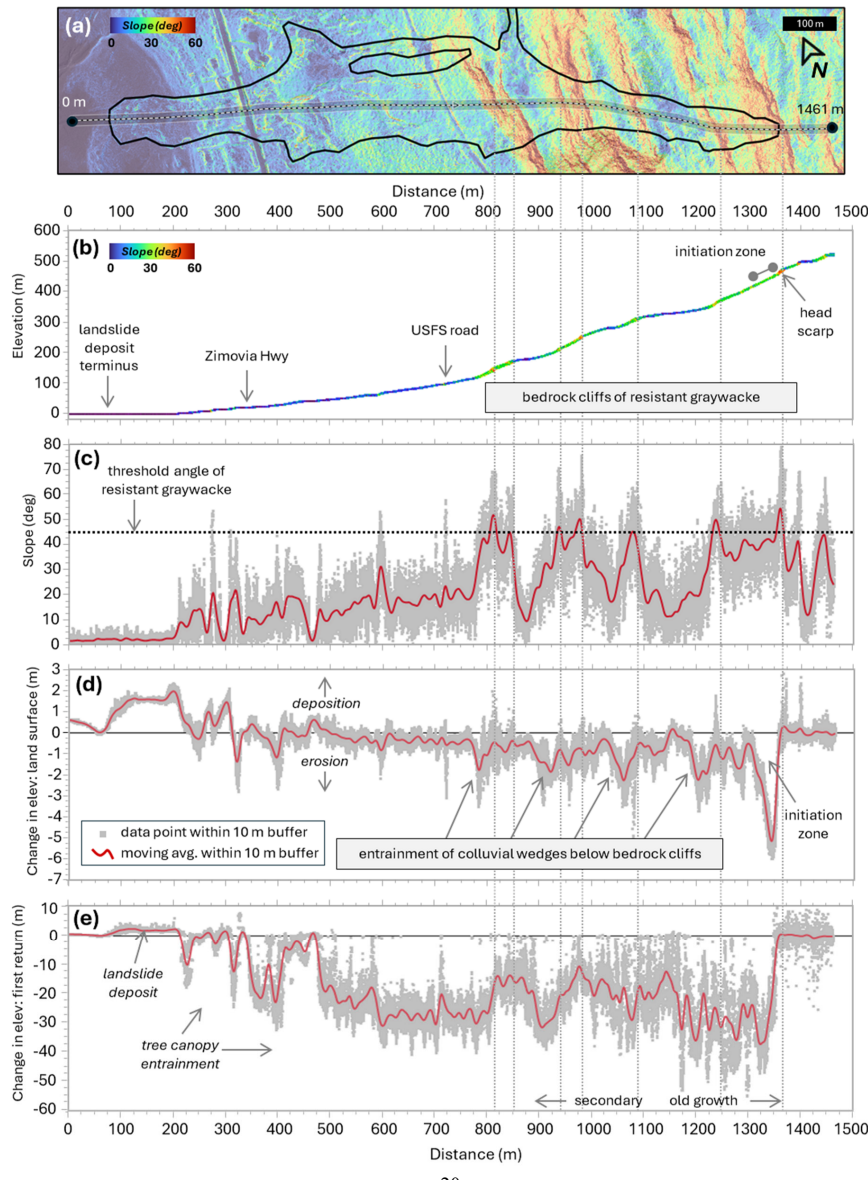
343 To assess the potential contribution from ridgeline wetlands and rapid snowmelt on the saturation of the initiation zone, we
344 mapped wetlands and hydrological flow paths upslope of the head scarp (Fig. 10a). Our map shows a radial drainage pattern
345 emanating from the ridgeline with an array of dispersed, west-directed flowpaths that drain to slide-prone slopes to the south
346 of the MP11.2 landslide (Fig. 10b). By contrast, flowpaths oriented to the north, east, and south tend to exhibit an incised and
347 well-defined channel network structure that is reflected by the narrow, dark blue (high drainage area) tendrils that contrast
348 with the more diffusive flowpaths with wider and lighter blue (lower drainage area) signatures draining west (Fig. 10b). This
349 pattern likely reflects the relative antiquity of channels and flowpaths draining from the ridgeline to the north, east, and south.
350 Notably, an elongate system of flowpaths is situated between the west- and north-directed drainages. This flow accumulation
351 pathway denoted by red arrows in Fig. 10b demarcates a substantial drainage area directed to the SE corner of the MP11.2
352 landslide head scarp and coincident with abundant seepage observed in the field. Our flow mapping indicates greater than
353 6,000 m² of drainage area upslope of the head scarp, and this source area includes a substantial fraction of low-gradient,
354 emergent wetlands with patchy bedrock exposure (Fig. 9b, 10a). In the field, this ridgeline wetland area (muskeg) was
355 characterized by deep (>2 m), organic soil akin to peatlands. Curiously, the flowpaths that contribute to the landslide head
356 scarp also reveal evidence of bifurcation into slide- and north-directed drainage systems (Fig. 10b). Our field observations
357 indicate that this bifurcation corresponds to meter-scale roughness in the bedrock/wetland surface, implying that the orientation
358 of ridgeline drainage may be highly dynamic and sensitive to local disturbances.

Formatted: Superscript

359 4.4 Landslide runout and mass balance

360 Our lidar and field analyses reveal strong topographic and geologic controls on the pattern of erosion and deposition along the
361 landslide runout path (Fig. 11). These analyses focus on the primary landslide path and do not include the north-directed
362 bifurcation that occurred in the middle sections and accounted for a small fraction of the slide volume. Our field observations
363 indicate that the initiation zone was localized to the upper 30 m (~1350 m on our transect; Fig. 11a) such that runout processes
364 are responsible for the downslope pattern of erosion and deposition. The W-NW directed path of the slide does not exhibit
365 topographic convergence as expressed by contour (or planform) curvature and thus lateral confinement did not affect the runout
366 behaviour. Rather, our 10-m wide swath-averaged transect data show that the lower half of the ~1,250-m long runout is
367 characterized by a low-gradient surface with slope angles that seldom exceed 20° (Fig. 11a-c). This zone of relatively gentle
368 topography coincides with our observations of nearshore/coastal deposits found at approximately 100 m above sea level. In
369 contrast, the upper half of the runout zone (between 800 and 1300 m along our transect) is characterized by a sequence of 5 to
370 7 step-bench segments (Fig. 11c). Steep cliffs of exposed bedrock are defined by east-dipping resistant graywacke beds that
371 manifest as continuous ledges across the landscape (Fig. 1). The intervening low-gradient (<20°) benches tend to be broad and
372 approximate bedding planes with a cap of locally derived colluvium. These steps composed of cliff-bench sequences are
373 ubiquitous in the marine sedimentary units across Wrangell Island and they are associated with numerous long-runout
374 landslides in the TNFLI.

375



377 **Figure 11.** Analysis of landslide properties along a 10-m wide longitudinal transect of the MP11.2 landslide. (a) Lidar map of
378 slope angle overlain on shaded relief map with transect location and endpoint distances depicted, (b) lidar-derived elevation
379 values from the November 2023 acquisition with points ~~colored~~ coloured by slope angle in degrees, (c) lidar-derived slope
380 angle, (d) DTM (or land surface) change, and (e) DSM (or canopy) change for all points within 10 meters of the transect
381 (~~gray~~ grey points) and running average (red line).

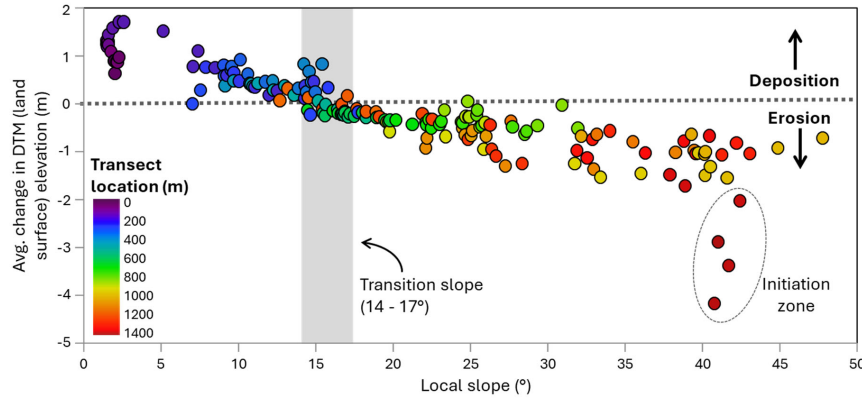
382

383 Our profile of DTM (or land surface) change shows that net erosion tends to dominate in the upper half of the landslide while
384 negligible net surface change and deposition characterize the lower half (Fig. 11d). The pattern of erosion in the upper half is
385 strongly correlated with the cliff-bench sequences. Specifically, local erosion maxima of 1 to 2 m (denoted by negative values
386 of surface change) span 25 to 50 m horizontally and occur just downslope of the steep bedrock cliffs where they transition to
387 the low-gradient benches (Fig. 11d). These foci of erosion coincide with field observations of colluvial wedges exposed along
388 the lateral margins of the landslide. Our analysis reveals minimal erosion along the low-gradient benches that are situated
389 below these colluvial wedges, and in the field these benches exhibited patchy entrainment as well as minor local deposition.
390 In the field, we also observed a live blueberry patch growing on a subvertical bedrock face at ~1000 m along the transect (Fig.
391 9c, 11c). This observation implies negligible erosion, and perhaps projectile behaviour of the landslide runout.

392 The profile of DSM (or canopy) change indicates removal of trees taller than 50 m in the upper 200 m of the initiation and
393 runout zones, whereas trees less than 40 m in height were mobilized from the lower area of the landslide (Fig. 11e). This
394 pattern results from pre-1965 timber harvests along the lower slopes in our study area with the transition to unmanaged forest
395 at 1,100 m along our transect (Fig. 11e). We sampled cookies from four western hemlock trees transported by the landslide
396 and deposited along the slide margins at approximately 900 m along our transect. The violent nature of the landslide snapped
397 the tree trunks, and we estimated that the lower 3 to 5 m of each trunk was missing. To account for the missing record, we
398 added 20 years to the age of each tree. The four trees ranged from 292 ± 10 to 322 ± 10 years old, indicating that they originated
399 from the old growth towards the top of the landslide. We also noted that reaction wood (which can be indicative of slope
400 movement) was present in all tree samples.

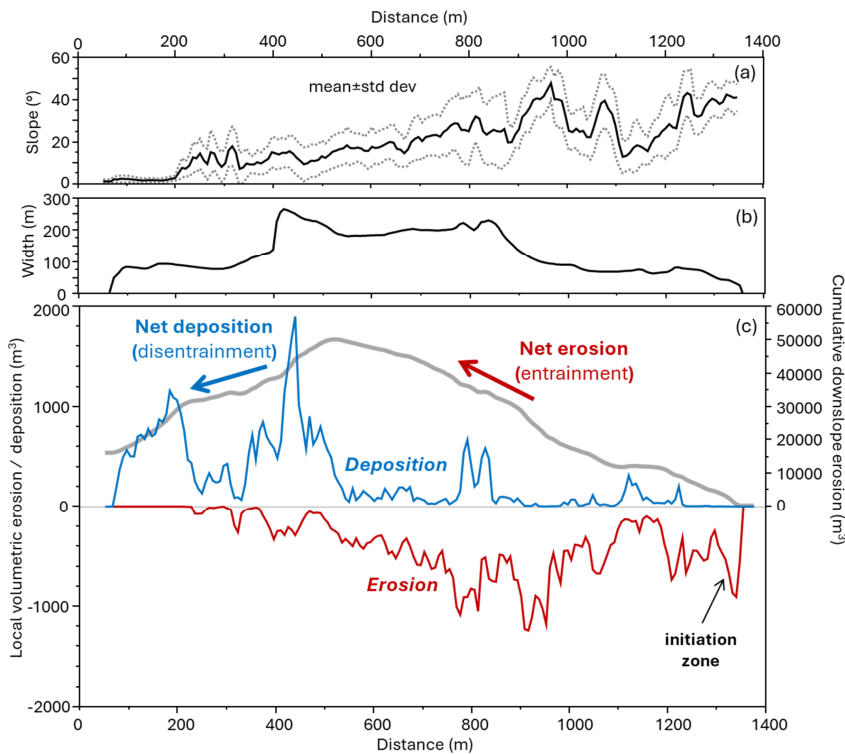
401 We plotted average surface or DTM change against local slope for 10-m intervals along the transect to assess mechanical
402 controls on debris flow entrainment and deposition (Fig. 12). Net erosion dominates when local slope exceeds 15° and the
403 average value of net erosion increases with slope from 15° to 45° . Notably, points defining this trend occur at a wide range of
404 locations along the transect, reflecting the profound influence of local slope on debris entrainment. That said, locations along
405 the middle section of the landslide, which are denoted by filled green circles (Fig. 12), tend to have lower values of net erosion
406 compared to upslope locations, which may result from variations in debris availability and saturation – or changing inertial
407 forces that control entrainment. For slopes between 41° and 44° , we observed several values of high net erosion (>3.2 m) that
408 deviate from the local slope-erosion trend. These values (denoted by dark red filled circles and a dashed ellipse in Fig. 12)
409 occur at the uppermost extent of the landslide and are associated with the initiation zone and thus reflect mechanical processes
410 that differ from downslope areas that experienced entrainment. For slope angles less than 15° we observe a trend of increasing

411 deposition with decreasing slope and a clustering of 0.7 to 1.7 m of deposition at 2° that defines the landslide toe. These trends
 412 define the slope-dependent transition between erosion and deposition for runout models, as well as provide constraints on
 413 entrainment potential.



414 **Figure 12.** Variation in local net erosion and deposition with slope angle. Values are averaged for 10-m bins along the transect
 415 in Fig. 11a. Colours reflect distance along the transect and the vertical grey rectangle denotes the transition slope between
 416 erosion and deposition. The dark red points enclosed by a dashed ellipse denote the initiation zone.
 417

418 We performed a mass balance of erosion and deposition along the MP11.2 landslide to identify the downslope transition of
 419 net erosion to deposition and quantify the total volume of erosion and deposition associated with the landslide (Fig. 13).
 420 Specifically, we tallied the total thickness of both erosion and deposition for all points within the landslide boundary using 10-
 421 m wide swaths oriented perpendicular to the longitudinal transect (Fig. 11a) and then separately summed the values within
 422 each swath. The distance between distal points on-along this transect defines the width of the landslide, which averaged less
 423 than 100 m in the upper 500 m of the slide, increased abruptly to greater than 200 m through the middle section, and then
 424 decreased to ~100 m in the lower depositional zone (Fig. 13b). Our mass balance analysis indicates high erosion at the initiation
 425 zone that decreased downslope before increasing rapidly just above the middle section, which coincides with landslide
 426 widening (red line in Fig. 13c). In the lower portions of the wide zone (400 to 500 m along the transect), we observe an abrupt
 427 transition from erosion (red line) to deposition (blue line) with a depositional peak that corresponds to the widest section of
 428 the landslide. In the field, this zone of localized widening corresponded with extensive accumulation of downed trees on the
 429 north flank of the landslide. Substantial deposition is associated with the landslide deposit (located between 75 and 250 m
 430 along the transect), just below a zone of local steepness (250 to 350 m along the transect) that experienced efficient transport
 431 and minimal deposition or erosion.
 432



433 **Figure 13.** Downslope mass balance analysis of the MP11.2 landslide. Profiles of (a) slope, (b) width, and (c) local erosion
434 (red), local deposition (blue), and cumulative erosion minus deposition (gray curve) calculated for all points within the
435 landslide boundaries along the transect in Fig. 11a. Note that the northward bifurcation pathway (Fig. 5a) is not included in
436 this analysis.

437

438 Lastly, we integrated total erosion and deposition along the landslide path by starting at the head scarp and summing the
439 imbalance in erosion (positive values of erosion) and deposition (negative values of erosion) in the downslope direction (see
440 grey curve in Fig. 13c), finishing at the slide terminus. Cumulative erosion increases monotonically in the downslope direction
441 before peaking at ~550 m along the transect. This implies an average volumetric growth factor of $62 m^3 m^{-1}$ along the erosional
442 portion of the landslide, although local variations associated with changes in slope occur. Downslope of the net erosion peak,
443 the slide widened and the slope became gentler, and as a result deposition outpaced erosion downslope. At the slide terminus,

444 the erosion-deposition balance did not approximate zero, however, indicating that net erosion exceeded deposition. In total,
445 we estimated 65,300 m³ of erosion and 49,400 m³ of deposition for the primary landslide, which implies an imbalance of
446 >15,000 m³ that may reflect debris loss in the coastal deposition zone as well as detection limits in depositional areas and
447 changes in bulk density. For the mass balance of the north-directed bifurcated portion of the landslide (Fig. 5c), we observed
448 4,000 m³ of erosion and 3,800 m³ of deposition.

449 **5 Discussion**

450 **5.1 Initiation and triggering factors**

451 Our preliminary investigation indicates that the MP11.2 landslide was an anomalously large and thus long-runout event that
452 initiated in a steep and wide deposit of thick colluvium during a notable but not atypical SE Alaska storm event. A wide range
453 of factors may have affected the initiation of the landslide and the uncertainty ascribed to our interpretations reflects limitations
454 in data availability, chiefly local climate observations, to test landslide initiation hypotheses. By contrast, geomorphic and
455 geologic factors that predisposed the hillslope to landsliding are more straightforward and provide important considerations
456 for the assessment of landslide hazard and risk in other locations.

457 Initiation of the MP11.2 landslide likely required a high degree of soil saturation to overcome the shear strength of the
458 colluvium and promote the observed highly mobile, fluid-like runout. The rainfall intensity that preceded the landslide was
459 notable but not extraordinary, as quantified by the 1-yr recurrence interval and 3-hr and 6-hr intensities recorded at Wrangell
460 airport. Given the 15-kilometer distance between the airport rain gauge and the landslide, and the greater than 400 m elevation
461 of the initiation zone, the rainfall experienced at MP11.2 is highly uncertain. During our community events, several residents
462 that drove along the Zimovia Highway on November 20 noted that rainfall south of Wrangell and closer to the landslide area
463 was more intense than in the town. In addition, several residents reported the presence of a substantial snowpack at mid- and
464 upper slope locations on the morning of November 20. At the airport weather station at sea level, air temperatures were cold
465 (~2°C) on November 19 and warmed rapidly on the morning of November 20, coincident with the arrival of abundant rainfall.
466 The temporal trend in air temperature at the initiation zone and ridgetop was likely similar although the absolute temperatures
467 were likely lower owing to the higher elevation. As a result, the rapid warming on November 20 combined with hours of
468 moderate-intensity rainfall may have generated substantial runoff via snowmelt. Days after a snow-dominated atmospheric
469 river, an extreme rain-dominated (1 in 500 yr event) atmospheric river generated widespread landslides and the fatal Beach
470 Road landslide in nearby Haines, AK, in December 2020. The scale and impact of these recent events suggest that the
471 sequencing and pacing of snow- and rain-dominated storms may be a critical factor in landslide initiation in SE Alaska. As
472 such, monitoring rain and snow in a wide range of settings is crucial for advancing our understanding of the hydrologic
473 response that contributes to landsliding.

474 The potential of high wind as a driver of recent landslides across SE Alaska, including the MP11. 2 event, has been surmised
475 by many residents. Tree turnover (or windthrow) can contribute to the initiation of shallow landslides and debris flows based

476 on observations from extreme storms (Guthrie et al., 2010; Lin et al., 2025). Such events tend to trigger widespread windthrow,
477 however, which was not observed on Wrangell Island during the November 20 storm. In the absence of tree turnover, the
478 potential for trees to transmit dynamic forces into the subsurface due to high winds has not been well-studied. Alternatively,
479 windthrow may impact slope stability through the reduction of root reinforcement (Parra et al., 2021). Pioneering research
480 documenting timber harvest impacts on slope stability was performed in SE Alaska on nearby Prince of Wales Island (Wu et
481 al., 1979) and those studies demonstrated the substantial contribution of soil shear strength through root reinforcement. More
482 recent advances highlight how the progressive tensile loading of root systems in shallow soils undergoing shear can be
483 quantified to assess slope stability in three dimensions, which is critical for capturing how roots reinforce the lateral margins
484 of potentially unstable slopes (Cohen et al., 2009). These studies demonstrate that as soils get thicker, the relative contribution
485 of root reinforcement to the total shear strength decreases substantially given that root density decreases exponentially with
486 depth (Schmidt et al., 2001). The root systems of coniferous forests tend to be concentrated in the upper 1 m (Hales, 2018;
487 Jackson et al., 1996) and as a result, root reinforcement was likely a minor contributor to the cumulative shear resistance of
488 the nearly 5-m thick initiation zone of the MP11.2 landslide. Nonetheless, the contribution may not be negligible, and further
489 analysis of the potential impact of the abating sawfly and budworm infestations on the root systems of western hemlock and
490 Sitka spruce trees in SE Alaska warrants further investigation. The infestation resulted in moderate-to-severe (11-50%)
491 mortality of infested trees on Wrangell Island and impacts are common on west-facing slopes and at elevations that coincide
492 with the initiation zone (U.S. Forest Service, 2025a).

493 Windy conditions can also contribute to landslide triggering through rapid snowmelt and excess runoff that occurs during
494 storms with high heat flux, which can be approximated as the product of mean daily temperature and wind speed (Hasebe and
495 Kumekawa, 1995). Recent analyses of atmospheric rivers have shown that these storms tend to be responsible for extreme
496 wind, as well as intense rainfall, and approximately half of the top 2% of wind speed events are associated with atmospheric
497 rivers (Waliser and Guan, 2017). Warm atmospheric rivers in the Sierra Nevada mountains, California, for example, have been
498 shown to generate a >1 km increase in the snow elevation over several hours, resulting in unanticipated excess discharge,
499 flooding, and mass movement events (Hatchett, 2018). In 2017, the contribution of extreme wind-driven snowmelt generated
500 a >35% increase in stream input to the Oroville Reservoir and the excess runoff resulted in overtopping flows and substantial
501 (>\\$1 billion) damage to the Oroville Dam as well as thousands of downstream evacuations (Henn et al., 2020). For the MP11.2
502 landslide, the abrupt rise in temperature and high winds on November 20 combined with the rapid disappearance of higher
503 elevation snowpack imply that wind-driven snowmelt may have contributed to the slope failure by generating excess runoff
504 and saturation of the initiation zone and downstream colluvial wedges. Most generally, the hydrologic status of colluvial
505 materials that were destabilized during the MP11.2 event evolved with the combined contributions of antecedent moisture,
506 rainfall, and snowmelt, although the relative importance of these three sources is unclear.

507 Our field observations of active seepage localized in the SE corner of the MP11.2 head scarp connected to a broad and gentle
508 ridgeline wetland suggests that the extent and character of terrain above steep slopes constitute a key control on landslide
509 susceptibility. Our mapping of hydrologic flowpaths along the ridgeline is consistent with these observations and implies that

510 subtle topographic variability may result in significant changes in the upslope or contributing area of landslide-prone slopes.
511 Similarly, a ponded topographic depression was mapped and monitored upslope of the 2020 Beach Road landslide and narrow
512 channels directly connected that area to the head scarp (Darrow et al., 2022). The abundance of these broad and gentle **ridgetops**
513 high elevation surfaces ([here](#) termed ridgeline water towers) is highly variable across SE Alaska and likely reflects variations
514 in glacial erosion and bedrock properties (Harris et al., 1974). Combining data from the national wetlands inventory with flow
515 routing analyses provides an opportunity to identify these ridgeline muskeg (or peatland) drainage systems and characterize
516 those with potential to influence hydrologic response on landslide-prone slopes. Because peatlands tend to experience rapid
517 saturation and flashy runoff, they are often sources of storm flow rather than attenuators of high flows (Holden, 2006). As a
518 result, their potential for contributing to landslide triggering demands investigation. Lidar data is a key requirement for
519 characterizing surface hydrology in these environments, and active monitoring of the drainage systems would help determine
520 the magnitude and timescale of hydrologic response and thus the potential contribution to slope instability.

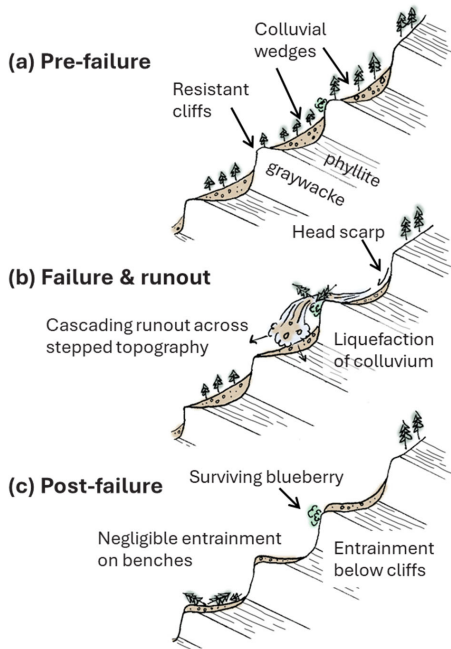
521 **5.2 Geologic and geomorphic factors that condition slopes for failure**

522 An additional factor predisposing the hillslopes above Zimovia Highway to landsliding is the accumulation of thick colluvium
523 that constitutes the initiation zone of the MP11.2 landslide as well as downslope material that enabled entrainment and
524 volumetric growth (or bulking) during runout. The thickness of colluvium varies substantially and systematically across the
525 hillslopes. In the field and from our lidar analyses, we observed extensive colluvial wedges draped below resistant graywacke
526 layers of the marine sedimentary unit. The punctuated pattern of downslope entrainment highlights how these colluvial wedges
527 contributed to the volumetric growth and broad area of inundation (Fig. 11d). We interpret these deposits to result from
528 progressive post-glacial rockfall locally derived from the resistant and underlying sedimentary layers.
529 The combination of east-dipping strata and a west-facing hillslope resulted in the observed pattern of bedrock ledges and thick
530 colluvial wedges that characterize much of the area, and we surmise that a non-negligible difference in bedrock strength may
531 be critical for setting up this geomorphic context. Our Schmidt hammer data highlight the high compressive strength of the
532 graywacke and weak strength of the fine-grained inner beds. At a quarry located just north of the landslide, we documented
533 bedrock structure and observed active slaking of the fine-grained inner beds that may destabilize the overlying resistant beds
534 ([supplementary materials](#)). Our kinematic analysis showing favourable conditions for flexural toppling is consistent with our
535 interpretation that progressive failure and retreat of the resistant ledges generate a wake of thick colluvium along the hillslopes
536 ([Imaizumi et al., 2015](#)). Importantly, these colluvial wedges will continue to form and thicken with on-going rockfall along
537 the resistant cliffs ([Moore et al., 2009](#)) although the pace and frequency of this process is unclear. In nearly all cases, the
538 colluvium is contained within the next downslope bench, which may provide a constraint on the pace of post-glacial bedrock
539 ledge failure and colluvium production. Examination of the TNFLI revealed dozens of other events on Wrangell Island that
540 occurred within a similar geomorphic context. Thus, changes in the bedrock dip and resistance, and slope orientation appear
541 to have a profound effect on the extent and thickness of the colluvial wedges that fuelled the MP11.2 landslide, although
542 further investigation is beyond the scope of this contribution.

543 **5.3 Controls on landslide runout and volumetric growth**

544 The large volume and extensive inundation area of the MP11.2 landslide likely originated from a thick and wide initiation
545 zone combined with the entrainment of abundant, saturated colluvium stored on downslope bedrock benches. In this area of
546 SE Alaska, post-glacial isostatic adjustment forms a fringe of uplifted, low-gradient terrain that may provide a key control on
547 landslide runout and deposition. In essence, many landslides on Wrangell and nearby islands appear to terminate upon reaching
548 this low-gradient terrain, when present. Exceptions include particularly large landslides, such as MP11.2, and slides that find
549 and follow confined flowpaths and behave as channelized debris flows. The MP11.2 landslide's depositional slope of 2° is
550 substantially lower than values observed on Prince of Wales and Baranof Islands that vary from 4° to 19° and 6° to 26°,
551 respectively (Booth et al., 2020; Johnson et al., 2000). Given that the mobility value ($H/L \sim 0.45$) for the MP11.2 slide is not
552 anomalous (Fig. 7a), we interpret its low deposit angle, and thus outsized and tragic impact, to result from highly efficient
553 entrainment and volumetric growth, which resulted in a large [volume and inundation area-and volume](#). Experimental and
554 theoretical investigations of debris flow runout emphasize that pore pressures generated as wet bed sediment is overridden and
555 progressively entrained, can reduce friction and facilitate increases in flow momentum (Iverson et al., 2011; Reid, 2011). These
556 studies emphasize that local slope and volumetric water content are highly sensitive factors that determine the extent of
557 entrainment during landslide runout (Iverson and Ouyang, 2015). Furthermore, because the colluvial stores on the slope were
558 emplaced by rockfall activity and soil transport, they may exist in a contractive state such that deformation and shearing
559 facilitate pore pressure development and volumetric growth.

560



561 **Figure 14.** Schematic of (a) pre-, (b) syn-, and (c) post-slide hillslope geometry, highlighting the influence of resistant bedrock
 562 and the downslope accumulation of colluvium that becomes mobilized during the landslide event. The live blueberry bush
 563 below a resistant bed reveals cascading, projectile-like behaviour of the slide material.

564

565 The volumetric growth factor of $62 \text{ m}^3 \text{ m}^{-1}$ is nearly 10x higher than typical values in unglaciated terrain (Reid et al., 2016),
 566 highlighting the importance of unconsolidated sediment thickness on steep slopes for determining landslide volume. From a
 567 mechanistic standpoint, the sequence of subvertical bedrock cliffs along the slide path also suggests that dynamic loading of
 568 stored colluvium from falling debris may have led to undrained loading and liquefaction (Collins and Reid, 2020). Thus, in
 569 contrast to check dams that are intended to attenuate momentum of flows in mountain channels (Remaître et al., 2008), the
 570 sequence of steps in the MP11.2 runout path may have instead facilitated momentum increases through a series of loading-
 571 induced liquefaction events (Fig. 14). This behaviour has been noted in other highly-mobile landslides with extensive
 572 inundation zones (Iverson et al., 2015). Lastly, the 15° slope angle that governs the transition between erosion and deposition
 573 along the MP11.2 landslide is steeper than values observed in unglaciated terrain that features valley confinement and thus

574 enables long runout debris flows (Reid et al., 2016). Acquiring estimates of this transition slope is important for implementing
575 landslide runout models, such as Laharz and GrfinTools (Brien et al., 2025) and will advance our ability to predict landslide
576 impacts in the region.

577 **6 Conceptual framework and research needs for shallow landslide assessment in SE Alaska**

578 Our analysis highlights key factors that govern the behaviour and hazard potential of shallow landslides in post-glacial
579 landscapes steeplands, such as SE Alaska.

580 • First, the accumulation of colluvium (or soil) on steep hillslopes serves as a key conditioning process for slope
581 instability. Previous studies in SE Alaska indicate typical landslide depths of 0.5 to 2.0 m and invoke in-situ
582 weathering of glacial till, soil creep, and tephra deposition as processes that generate material of sufficient thickness
583 to initiate shallow landslides (Swanson, 1970). Here, we identify deposition of thick colluvial wedges below resistant
584 bedrock cliffs as an additional contributor, although the relative importance of these processes remains unclear. More
585 generally, the timescale of processes that generate colluvium dictates the frequency, magnitude, and spatial pattern
586 of landsliding in post-glacial landscapes although relevant data are limited.

587 • Second, characterizing water sources and flow accumulation above landslide-prone hillslopes will facilitate the
588 identification of terrain with high hazard potential. Many glaciated mountains feature broad, gentle ridgetops that can
589 store and convey large quantities of surface and near-surface water, particularly during snowmelt and rain-on-snow
590 events. In British Columbia, this terrain is termed “gentle-over-steep” (Jordan, 2016) and efforts to characterize and
591 map these particular landforms and quantify drainage patterns using airborne lidar data should be a research priority
592 in SE Alaska.

593 • Third, the runout of debris flows and debris avalanches in SE Alaska is seldom facilitated by channels or
594 topographic confinement. Rather, most landslides navigate poorly-dissected, post-glacial terrain, and the prediction
595 of debris flow runout in these settings is challenging owing to highly-variable resistance in the form of vegetation and
596 flow materials. In these post-glacial settings, the parameters for empirical models (such as the erosion-deposition
597 transition angle) have not been constrained and the ability of these models to account for controls on runout is
598 untested. Physically-based models that account for how large wood and variable grain size dictate flow behaviour
599 also merit further investigation in conjunction with landslide inventory data and field observations.

600 • Fourth, because debris flow volume is the primary control on inundation area, quantification of entrainment along
601 slide paths is essential for runout modelling. The availability of colluvium and its relative saturation can promote
602 entrainment. Spatial and temporal variations in these two factors likely depend on the pace and pattern of post-glacial
603 landscape evolution that determines where colluvium accumulates and how hillslope drainage paths are organized.
604 Thus, landscape evolution models that are developed and tested in postglacial settings should be a research priority.

605 • Lastly, although atmospheric rivers have been responsible for all the recent fatal landslide events in SE Alaska, the
606 character and relative magnitude of these ARs have been highly variable. Some have been notable for producing ~~a~~
607 fewseveral hours of intense rainfall while others have been characterized by protracted rain-on-snow. Thus,
608 quantifying how the sequencing and character of ARs affects landslide susceptibility will be a key component of
609 efforts to build a landslide warning system (Nash et al., 2024). Currently, the region lacks sufficient weather station
610 observations and climate reanalysis productions (Lader et al., 2020) are limited in scope and resolution.

611 Most generally, advancing our understanding of how these geomorphic and atmospheric processes contribute to slope
612 instability across SE Alaska will inform how we assess, plan, mitigate, and manage landslide hazards and minimize impacts
613 on public safety and infrastructure.

614 7 Conclusions

615 The 2023 Wrangell Island landslide was among the most impactful and deadly in Southeast Alaska's recent history and reveals
616 critical insights into shallow landslide processes in post-glacial terrain. Our investigation demonstrates how geological
617 structure, post-glacial landscape evolution, hydrologic connectivity, and atmospheric forcing combined to produce a high-
618 impact event with devastating consequences. Although rainfall intensity during the triggering storm was relatively modest, the
619 landslide magnitude and impact were amplified by several preconditioning factors that are poorly represented with existing
620 conceptual models and hazard frameworks.

621 Our key findings include the following:

- 622 • Evidence of windthrow contributing to the slope failure is lacking, but rain-on-snow dynamics facilitated by ← - -
623 high wind and warm air temperatures may have delivered critical runoff not captured by typical rainfall intensity
624 metrics.
- 625 • Ridgetop wetlands with subtle drainage divides control hydrologic routing to many landslide-prone slopes,
626 concentrating surface flowpaths and downslope slope saturation.
- 627 • Thick colluvial wedges, perched below resistant bedrock ledges, provided an abundant source zone of readily
628 mobilized material that fuelled entrainment and long runout.
- 629 • The transition between erosion and deposition along the stepped flowpath occurred at 15° regardless of position
630 along the transect, reflecting the profound influence of local slope angle on sediment entrainment.
- 631 • Stepped topography acted to maintain flow momentum, enabling progressive entrainment and promoting
632 mobility.
- 633 • Sequential lidar and flow modelling are essential tools for identifying landslide initiation susceptibility,
634 erosion/deposition patterns, and geomorphic preconditioning.
- 635 • Large, high mobility shallow landslides can occur on anti-dip hillslopes and risk may be greater than previously
636 recognized.

Formatted: List Paragraph, Bulleted + Level: 1 + Aligned at: 0.5" + Indent at: 0.75"

637 These findings highlight high key knowledge gaps and can guide future risk mitigation and early warning strategies in steep,
638 post-glacial landscapes. Specifically, advancing landslide prediction in SE Alaska requires expanded lidar coverage, integrated
639 snow and rainfall monitoring, climate modelling, and advances in the modelling of post-glacial landscape evolution,
640 weathering, and colluvium thickness that provide the means for landslide initiation and entrainment.

641 **Author contributions**

642 MD wrote the proposal and planned the campaign; MD, JR, AP, and AJ performed the fieldwork; ~~AP and MD contributed~~
643 ~~figures and analyses~~; MD collected and analysed the soil and tree samples; JR performed the topographic, climate, and
644 inventory analyses; JR wrote the manuscript draft; MD, JR, AP, and AJ reviewed and edited the manuscript; ~~AP and MD~~
645 contributed figures and analyses.

646 **Acknowledgments**

647 The authors thank the National Science Foundation (RAPID EAR Award 2421234 to University of Alaska-Fairbanks) for
648 supporting this work, Wrangell Cooperative Association for partnership and knowledge sharing, City of Wrangell staff for
649 resources, discussions, and maps, S. and G. Helgesen for access, A. Park and A. Edwards for fieldwork contributions, A.
650 O'Brien and T. Belback for ~~their excellent~~ sawyer services, ~~and~~ Nolan Center staff for hosting multiple community events,
651 and ~~and~~ M. Sanders, M. Reid, D. Staley, K. Barnhart, T. Eckhoff, K. Prussian, J. Foss, S. McKay, J. Montigny, and T. Wetor for
652 insightful conversations.

653 **References**

654 Alaska Department of Transportation and Public Facilities: Alaska Test Methods Manual: ADOT&PF, 2023.

655 American Society for Testing Materials: Standard Test Method for Determination of Rock Hardness by Rebound Hammer
656 Method, 2014a.

657 American Society for Testing Materials: Standard Test Methods for Specific Gravity of Soil Solids by Water Pycnometer,
658 2014b.

659 American Society for Testing Materials: Standard Practice for Classification of Soils for Engineering Purposes (Unified Soil
660 Classification System), 2017a.

661 American Society for Testing Materials: Standard Test Methods for Particle-Size Distribution (Gradation) of Soils Using Sieve
662 Analysis, 2017b.

663 American Society for Testing Materials: Standard Test Method for Particle-Size Distribution (Gradation) of Fine-Grained
664 Soils Using the Sedimentation (Hydrometer) Analysis, 2021.

665 Aydin, A. and Basu, A.: The Schmidt hammer in rock material characterization, *Engineering Geology*, 81, 1–14,
666 <https://doi.org/10.1016/j.enggeo.2005.06.006>, 2005.

667 Baichtal, J. F., Lesnek, A. J., Carlson, R. J., Schmuck, N. S., Smith, J. L., Landwehr, D. J., and Briner, J. P.: Late Pleistocene
668 and early Holocene sea-level history and glacial retreat interpreted from shell-bearing marine deposits of southeastern Alaska,
669 USA, *Geosphere*, 17, 1590–1615, <https://doi.org/10.1130/GES02359.1>, 2021.

670 Benda, L. and Dunne, T.: Stochastic forcing of sediment supply to channel networks from landsliding and debris flow, *Water
671 Resources Research*, 33, 2849–2863, <https://doi.org/10.1029/97WR02388>, 1997.

672 Booth, A. M., Sifford, C., Vascik, B., Siebert, C., and Buma, B.: Large wood inhibits debris flow runout in forested southeast
673 Alaska, *Earth Surface Processes and Landforms*, n/a, <https://doi.org/10.1002/esp.4830>, 2020.

674 Booth, A. M., Buma, B., and Nagorski, S.: Effects of Landslides on Terrestrial Carbon Stocks With a Coupled Geomorphic-
675 Biologic Model: Southeast Alaska, United States, *Journal of Geophysical Research: Biogeosciences*, 128, e2022JG007297,
676 <https://doi.org/10.1029/2022JG007297>, 2023.

677 Bovy, B., Braun, J., and Demoulin, A.: A new numerical framework for simulating the control of weather and climate on the
678 evolution of soil-mantled hillslopes, *Geomorphology*, 263, 99–112, <https://doi.org/10.1016/j.geomorph.2016.03.016>, 2016.

679 Brardinoni, F. and Hassan, M. A.: Glacial erosion, evolution of river long profiles, and the organization of process domains in
680 mountain drainage basins of coastal British Columbia, *Journal of Geophysical Research*, 111,
681 <https://doi.org/10.1029/2005JF000358>, 2006.

682 Brardinoni, F., Hassan, M. A., Rollerson, T., and Maynard, D.: Colluvial sediment dynamics in mountain drainage basins,
683 *Earth and Planetary Science Letters*, 284, 310–319, <https://doi.org/10.1016/j.epsl.2009.05.002>, 2009.

684 Brardinoni, F., Picotti, V., Maraio, S., Bruno, P. P., Cucato, M., Morelli, C., and Mair, V.: Postglacial evolution of a formerly
685 glaciated valley: Reconstructing sediment supply, fan building, and confluence effects at the millennial time scale, *GSA
686 Bulletin*, 130, 1457–1473, <https://doi.org/10.1130/B31924.1>, 2018.

687 Brien, D. L., Reid, M. E., Cronkite-Ratcliff, C., and Perkins, J. P.: Topographic controls on landslide mobility: modeling
688 hurricane-induced landslide runout and debris-flow inundation in Puerto Rico, *Natural Hazards and Earth System Sciences*,
689 25, 1229–1253, <https://doi.org/10.5194/nhess-25-1229-2025>, 2025.

690 Buma, B. and Johnson, A. C.: The role of windstorm exposure and yellow cedar decline on landslide susceptibility in southeast
691 Alaskan temperate rainforests, *Geomorphology*, 228, 504–511, <https://doi.org/10.1016/j.geomorph.2014.10.014>, 2015.

692 Buma, B. and Pawlik, L.: Post-landslide soil and vegetation recovery in a dry, montane system is slow and patchy, *Ecosphere*,
693 12, <https://doi.org/10.1002/ecs2.3346>, 2021.

694 Carrara, P. E., Ager, T. A., Baichtal, J. F., and VanSistine, D. P.: Map of glacial limits and possible refugia in the southern
695 Alexander Archipelago, Alaska, during the late Wisconsin glaciation, *Miscellaneous Field Studies Map*,
696 <https://doi.org/10.3133/mf2424>, 2003.

697 Cohen, D., Lehmann, P., and Or, D.: Fiber bundle model for multiscale modeling of hydromechanical triggering of shallow
698 landslides, *Water Resources Research*, 45, <https://doi.org/10.1029/2009WR007889>, 2009.

699 Collins, B. D. and Reid, M. E.: Enhanced landslide mobility by basal liquefaction: The 2014 State Route 530 (Oso),
700 Washington, landslide, *GSA Bulletin*, 132, 451–476, <https://doi.org/10.1130/B35146.1>, 2020.

701 Cordeira, J. M., Stock, J., Dettinger, M. D., Young, A. M., Kalansky, J. F., and Ralph, F. M.: A 142-year Climatology of
702 Northern California Landslides and Atmospheric Rivers, *Bulletin of the American Meteorological Society*, BAMS-D-18-
703 0158.1, <https://doi.org/10.1175/BAMS-D-18-0158.1>, 2019.

704 Darrow, M. M., Nelson, V. A., Grilliot, M., Wartman, J., Jacobs, A., Baichtal, J. F., and Buxton, C.: Geomorphology and
705 initiation mechanisms of the 2020 Haines, Alaska landslide, *Landslides*, <https://doi.org/10.1007/s10346-022-01899-3>, 2022.

706 DiBiase, R. A., Lamb, M. P., Ganti, V., and Booth, A. M.: Slope, grain size, and roughness controls on dry sediment transport
707 and storage on steep hillslopes: PARTICLE TRANSPORT ON STEEP HILLSLOPES, *Journal of Geophysical Research: Earth Surface*, 122, 941–960, <https://doi.org/10.1002/2016JF003970>, 2017.

709 Dietrich, W. E., Wilson, C. J., and Reneau, S. L.: Hollows, colluvium, and landslides in soil-mantled landscapes, in: *Hillslope
710 Processes*, edited by: Abrahams, A. D., Routledge, 362–388, <https://doi.org/10.4324/9781003028840-17>, 1986.

711 Dietrich, W. E., Reiss, R., Hsu, M., and Montgomery, D. R.: A process-based model for colluvial soil depth and shallow
712 landsliding using digital elevation data, *Hydrological Processes*, 9, 383–400, <https://doi.org/10.1002/hyp.3360090311>, 1995.

713 D'Odorico, P. and Fagherazzi, S.: A probabilistic model of rainfall-triggered shallow landslides in hollows: A long-term
714 analysis, *Water Resources Research*, 39, <https://doi.org/10.1029/2002WR001595>, 2003.

715 Fan, L., Lehmann, P., Zheng, C., and Or, D.: Rainfall Intensity Temporal Patterns Affect Shallow Landslide Triggering and
716 Hazard Evolution, *Geophysical Research Letters*, 47, e2019GL085994, <https://doi.org/10.1029/2019GL085994>, 2020.

717 Flagstad, L., Steer, A., Boucher, T., Aisu, M., and Lema, P.: Wetlands across Alaska: Statewide wetland map and Assessment
718 of rare wetland ecosystems, 2018.

719 Gabet, E. J. and Mudd, S. M.: The mobilization of debris flows from shallow landslides, *Geomorphology*, 74, 207–218,
720 <https://doi.org/10.1016/j.geomorph.2005.08.013>, 2006.

721 Godt, J. W., Wood, N. J., Pennaz, A. B., Dacey, C. M., Mirus, B. B., Schaefer, L. N., and Slaughter, S. L.: National strategy
722 for landslide loss reduction, Open-File Report, U.S. Geological Survey, <https://doi.org/10.3133/ofr20221075>, 2022.

723 Goetz, J. N., Guthrie, R. H., and Brenning, A.: Forest harvesting is associated with increased landslide activity during an
724 extreme rainstorm on Vancouver Island, Canada, *Natural Hazards and Earth System Sciences*, 15, 1311–1330,
725 <https://doi.org/10.5194/nhess-15-1311-2015>, 2015.

726 Gonzalez de Vallejo, L. and Ferrer, M.: *Geological Engineering*, CRC Press, London, 700 pp., <https://doi.org/10.1201/b11745>,
727 2011.

728 Gorr, A. N., McGuire, L. A., Youberg, A. M., and Rengers, F. K.: A progressive flow-routing model for rapid assessment of
729 debris-flow inundation, *Landslides*, 19, 2055–2073, <https://doi.org/10.1007/s10346-022-01890-y>, 2022.

730 Guan, B., Waliser, D. E., Ralph, F. M., Fetzer, E. J., and Neiman, P. J.: Hydrometeorological characteristics of rain-on-snow
731 events associated with atmospheric rivers, *Geophysical Research Letters*, 43, 2964–2973,
732 <https://doi.org/10.1002/2016GL067978>, 2016.

733 Guilinger, J. J., Foufoula-Georgiou, E., Gray, A. B., Randerson, J. T., Smyth, P., Barth, N. C., and Goulden, M. L.: Predicting
734 Postfire Sediment Yields of Small Steep Catchments Using Airborne Lidar Differencing, *Geophysical Research Letters*, 50,
735 e2023GL104626, <https://doi.org/10.1029/2023GL104626>, 2023.

736 Guthrie, R. H.: The effects of logging on frequency and distribution of landslides in three watersheds on Vancouver Island,
737 British Columbia, *Geomorphology*, 43, 273–292, [https://doi.org/10.1016/S0169-555X\(01\)00138-6](https://doi.org/10.1016/S0169-555X(01)00138-6), 2002.

738 Guthrie, R. H., Mitchell, S. J., Lanquaye-Opoku, N., and Evans, S. G.: Extreme weather and landslide initiation in coastal
739 British Columbia, *Quarterly Journal of Engineering Geology and Hydrogeology*, 43, 417–428, <https://doi.org/10.1144/1470-9236/08-119>, 2010.

741 Haeussler, P. J.: Structural evolution of an arc-basin: The Gravina Belt in central southeastern Alaska, *Tectonics*, 11, 1245–
742 1265, <https://doi.org/10.1029/92TC01107>, 1992.

743 Hales, T. C.: Modelling biome-scale root reinforcement and slope stability, *Earth Surface Processes and Landforms*, 43, 2157–
744 2166, <https://doi.org/10.1002/esp.4381>, 2018.

745 Hamilton, T. D.: Late Cenozoic glaciation of Alaska, in: *The Geology of Alaska*, vol. G-1, edited by: Plafker, G. and Berg, H.
746 C., Geological Society of America, 0, <https://doi.org/10.1130/DNAG-GNA-G1.813>, 1994.

747 Harris, A. S. and Farr, W. A.: The forest ecosystem of southeast Alaska: 7. Forest ecology and timber management., Gen.
748 Tech. Rep. PNW-GTR-025. Portland, OR: U.S. Department of Agriculture, Forest Service, Pacific Northwest Research
749 Station. 116 p, 025, 1974.

750 Harris, A. S., Hutchison, K., Meehan, W. R., Swanston, D. N., Helmers, A. E., Hendee, J. C., and Collins, T. M.: *THE FOREST
751 ECOSYSTEM OF SOUTHEAST ALASKA I. The Setting*, USDA, Portland, OR, 1974.

752 Hasebe, M. and Kumekawa, T.: Estimation of snowmelt volume using air temperature and wind speed, *Environment
753 International*, 21, 497–500, [https://doi.org/10.1016/0160-4120\(95\)00048-P](https://doi.org/10.1016/0160-4120(95)00048-P), 1995.

754 Hatchett, B. J.: Snow Level Characteristics and Impacts of a Spring Typhoon-Originating Atmospheric River in the Sierra
755 Nevada, USA, *Atmosphere*, 9, 233, <https://doi.org/10.3390/atmos9060233>, 2018.

756 Hees, W. W. S. van and Mead, B. R.: Extensive, strategic assessment of southeast Alaska's vegetative resources., *Landscape
757 and Urban Planning*, 72: 25–48, <https://doi.org/10.1016/j.landurbplan.2004.09.027>, 2005.

758 Henn, B., Musselman, K. N., Lestak, L., Ralph, F. M., and Molotch, N. P.: Extreme Runoff Generation From Atmospheric
759 River Driven Snowmelt During the 2017 Oroville Dam Spillways Incident, *Geophysical Research Letters*, 47,
760 e2020GL088189, <https://doi.org/10.1029/2020GL088189>, 2020.

761 Holden, J.: Chapter 14 Peatland hydrology, in: *Developments in Earth Surface Processes*, vol. 9, edited by: Martini, I. P.,
762 Martínez Cortizas, A., and Chesworth, W., Elsevier, 319–346, [https://doi.org/10.1016/S0928-2025\(06\)09014-6](https://doi.org/10.1016/S0928-2025(06)09014-6), 2006.

763 Hovius, N., Stark, C. P., and Allen, P. A.: Sediment flux from a mountain belt derived by landslide mapping, *Geology*, 25,
764 231, [https://doi.org/10.1130/0091-7613\(1997\)025%253C0231:SFFAMB%253E2.3.CO;2](https://doi.org/10.1130/0091-7613(1997)025%253C0231:SFFAMB%253E2.3.CO;2), 1997.

765 Howe, M., Graham, E. E., and Nelson, K. N.: Defoliator outbreaks track with warming across the Pacific coastal temperate
766 rainforest of North America, *Ecography*, 2024, e07370, <https://doi.org/10.1111/ecog.07370>, 2024.

767 Imaizumi, F., Nishii, R., Murakami, W., and Daimaru, H.: Parallel retreat of rock slopes underlain by alternation of strata,
768 *Geomorphology*, 238, 27–36, <https://doi.org/10.1016/j.geomorph.2015.02.030>, 2015.

769 Iverson, R. M.: Landslide triggering by rain infiltration, *Water Resour. Res.*, 36, 1897–1910,
770 <https://doi.org/10.1029/2000WR900090>, 2000.

771 Iverson, R. M. and Ouyang, C.: Entrainment of bed material by Earth-surface mass flows: Review and reformulation of depth-
772 integrated theory: Entrainment of bed material, *Reviews of Geophysics*, 53, 27–58, <https://doi.org/10.1002/2013RG000447>,
773 2015.

774 Iverson, R. M., Reid, M. E., Logan, M., LaHusen, R. G., Godt, J. W., and Griswold, J. P.: Positive feedback and momentum
775 growth during debris-flow entrainment of wet bed sediment, *Nature Geosci*, 4, 116–121, <https://doi.org/10.1038/ngeo1040>,
776 2011.

777 Iverson, R. M., George, D. L., Allstadt, K., Reid, M. E., Collins, B. D., Vallance, J. W., Schilling, S. P., Godt, J. W., Cannon,
778 C. M., Magirl, C. S., Baum, R. L., Coe, J. A., Schulz, W. H., and Bower, J. B.: Landslide mobility and hazards: implications
779 of the 2014 Oso disaster, *Earth and Planetary Science Letters*, 412, 197–208, <https://doi.org/10.1016/j.epsl.2014.12.020>, 2015.

780 Jackson, R. B., Canadell, J., Ehleringer, J. R., Mooney, H. A., Sala, O. E., and Schulze, E. D.: A global analysis of root
781 distributions for terrestrial biomes, *Oecologia*, 108, 389–411, <https://doi.org/10.1007/BF00333714>, 1996.

782 Johnson, A. C., Swanston, D. N., and McGee, K. E.: Landslide initiation, runout, and deposition within clearcuts and old-
783 growth forests of Alaska, *J American Water Resour Assoc*, 36, 17–30, <https://doi.org/10.1111/j.1752-1688.2000.tb04245.x>,
784 2000.

785 Jordan, P.: Post-wildfire debris flows in southern British Columbia, Canada, *Int. J. Wildland Fire*, 25, 322,
786 <https://doi.org/10.1071/WF14070>, 2016.

787 Karl, S. M., Haeussler, P. J., and Mccafferty, A. E.: Reconnaissance Geologic Map of the Duncan Canal/Zarembo Island Area,
788 Southeastern Alaska, Reston, VA, 1999.

789 Korup, O., Densmore, A. L., and Schlunegger, F.: The role of landslides in mountain range evolution, *Geomorphology*, 120,
790 77–90, <https://doi.org/10.1016/j.geomorph.2009.09.017>, 2010.

791 Lader, R., Bidlack, A., Walsh, J. E., Bhatt, U. S., and Bieniek, P. A.: Dynamical Downscaling for Southeast Alaska: Historical
792 Climate and Future Projections, <https://doi.org/10.1175/JAMC-D-20-0076.1>, 2020.

793 Lamb, M. P., Scheingross, J. S., Amidon, W. H., Swanson, E., and Limaye, A.: A model for fire-induced sediment yield by
794 dry ravel in steep landscapes, *Journal of Geophysical Research*, 116, <https://doi.org/10.1029/2010JF001878>, 2011.

795 Lancaster, S. T., Hayes, S. K., and Grant, G. E.: Effects of wood on debris flow runout in small mountain watersheds:
796 EFFECTS OF WOOD ON DEBRIS FLOW RUNOUT, *Water Resources Research*, 39,
797 <https://doi.org/10.1029/2001WR001227>, 2003.

798 Larsen, I. J., Montgomery, D. R., and Korup, O.: Landslide erosion controlled by hillslope material, *Nature Geoscience*, 3,
799 247–251, <https://doi.org/10.1038/ngeo776>, 2010.

800 Lempert, R. J., Busch, L., Brown, R., Patton, A., Turner, S., Schmidt, J., and Young, T.: Community-Level, Participatory Co-
801 Design for Landslide Warning with Implications for Climate Services, *Sustainability*, 15, 4294,
802 <https://doi.org/10.3390/su15054294>, 2023.

803 Lin, Y.-C., Hsieh, J.-Y., Shih, H.-S., and Wang, W.-H.: Strong wind is one of the important factors that trigger landslides, *npj
804 Nat. Hazards*, 2, 12, <https://doi.org/10.1038/s44304-025-00062-x>, 2025.

805 Mann, D. H. and Hamilton, T. D.: Late Pleistocene and Holocene paleoenvironments of the North Pacific coast, *Quaternary
806 Science Reviews*, 14, 449–471, [https://doi.org/10.1016/0277-3791\(95\)00016-I](https://doi.org/10.1016/0277-3791(95)00016-I), 1995.

807 Marra, F., Armon, M., and Morin, E.: Coastal and orographic effects on extreme precipitation revealed by weather radar
808 observations, *Hydrology and Earth System Sciences*, 26, 1439–1458, <https://doi.org/10.5194/hess-26-1439-2022>, 2022.

809 Menounos, B., Goehring, B. M., Osborn, G., Margold, M., Ward, B., Bond, J., Clarke, G. K. C., Clague, J. J., Lakeman, T.,
810 Koch, J., Caffee, M. W., Gosse, J., Stroeven, A. P., Seguinot, J., and Heyman, J.: Cordilleran Ice Sheet mass loss preceded
811 climate reversals near the Pleistocene Termination, *Science*, 358, 781–784, <https://doi.org/10.1126/science.aan3001>, 2017.

812 Montgomery, D. R., Dietrich, W. E., Torres, R., Anderson, S. P., Heffner, J. T., and Loague, K.: Hydrologic response of a
813 steep, unchanneled valley to natural and applied rainfall, *Water Resour. Res.*, 33, 91–109, <https://doi.org/10.1029/96WR02985>,
814 1997.

815 Moore, J. R., Sanders, J. W., Dietrich, W. E., and Glaser, S. D.: Influence of rock mass strength on the erosion rate of alpine
816 cliffs, *Earth Surface Processes and Landforms*, 34, 1339–1352, <https://doi.org/10.1002/esp.1821>, 2009.

817 Nash, D., Rutz, J. J., and Jacobs, A.: Atmospheric Rivers in Southeast Alaska: Meteorological Conditions Associated With
818 Extreme Precipitation, *Journal of Geophysical Research: Atmospheres*, 129, e2023JD039294,
819 <https://doi.org/10.1029/2023JD039294>, 2024.

820 National Oceanographic and Atmospheric Administration (NOAA): NOWData – NOAA Online Weather Data, 2024.

821 Neiman, P. J., Ralph, F. M., Wick, G. A., Lundquist, J. D., and Dettinger, M. D.: Meteorological Characteristics and Overland
822 Precipitation Impacts of Atmospheric Rivers Affecting the West Coast of North America Based on Eight Years of SSM/I
823 Satellite Observations, *Journal of Hydrometeorology*, 9, 22–47, <https://doi.org/10.1175/2007JHM855.1>, 2008.

824 Nicolazzo, J. A., Wikstrom Jones, K. M., Salisbury, J. B., and Horen, K. C.: Post-landslide elevation changes detected from
825 multi-temporal lidar surveys of the November 2023 Wrangell, Alaska, landslides, Alaska Division of Geological &
826 Geophysical Surveys, <https://doi.org/10.14509/31124>, 2024.

827 Oakley, N. S., Lancaster, J. T., Hatchett, B. J., Stock, J., Ralph, F. M., Roj, S., and Lukashov, S.: A 22-Year Climatology of
828 Cool Season Hourly Precipitation Thresholds Conducive to Shallow Landslides in California, *Earth Interact.*, 22, 1–35,
829 <https://doi.org/10.1175/EI-D-17-0029.1>, 2018.

830 Parra, E., Mohr, C. H., and Korup, O.: Predicting Patagonian Landslides: Roles of Forest Cover and Wind Speed, *Geophysical
831 Research Letters*, 48, e2021GL095224, <https://doi.org/10.1029/2021GL095224>, 2021.

832 Patton, A. I., Roering, J. J., and Orland, E.: Debris flow initiation in postglacial terrain: Insights from shallow landslide
833 initiation models and geomorphic mapping in Southeast Alaska, *Earth Surface Processes and Landforms*, n/a,
834 <https://doi.org/10.1002/esp.5336>, 2022.

835 Patton, A. I., Luna, L. V., Roering, J. J., Jacobs, A., Korup, O., and Mirus, B. B.: Landslide initiation thresholds in data-sparse
836 regions: application to landslide early warning criteria in Sitka, Alaska, USA, *Natural Hazards and Earth System Sciences*, 23,
837 3261–3284, <https://doi.org/10.5194/nhess-23-3261-2023>, 2023.

838 Ralph, F. M., Neiman, P. J., and Wick, G. A.: Satellite and CALJET Aircraft Observations of Atmospheric Rivers over the
839 Eastern North Pacific Ocean during the Winter of 1997/98, 2004.

840 Reid, M. E.: Entrainment of bed sediment by debris flows : results from large-scale experiments, *Italian Journal of Engineering
841 Geology and Environment*, 367–374, <https://doi.org/10.4408/IJEGE.2011-03.B-042>, 2011.

842 Reid, M. E., Coe, J. A., and Brien, D. L.: Forecasting inundation from debris flows that grow volumetrically during travel,
843 with application to the Oregon Coast Range, USA, *Geomorphology*, 273, 396–411,
844 <https://doi.org/10.1016/j.geomorph.2016.07.039>, 2016.

845 Remaître, A., van Asch, T. W. J., Malet, J.-P., and Maquaire, O.: Influence of check dams on debris-flow run-out intensity,
846 *Natural Hazards and Earth System Sciences*, 8, 1403–1416, <https://doi.org/10.5194/nhess-8-1403-2008>, 2008.

847 Rengers, F. K., Kean, J. W., Reitman, N. G., Smith, J. B., Coe, J. A., and McGuire, L. A.: The Influence of Frost Weathering
848 on Debris Flow Sediment Supply in an Alpine Basin, *Journal of Geophysical Research: Earth Surface*, 125, e2019JF005369,
849 <https://doi.org/10.1029/2019JF005369>, 2020.

850 Rickenmann, D.: Empirical Relationships for Debris Flows, *Natural Hazards*, 19, 47–77,
851 <https://doi.org/10.1023/A:1008064220727>, 1999.

852 Rulli, M. C., Meneguzzo, F., and Rosso, R.: Wind control of storm-triggered shallow landslides, *Geophysical Research Letters*,
853 34, <https://doi.org/10.1029/2006GL028613>, 2007.

854 Schmidt, K. M., Roering, J. J., Stock, J. D., Dietrich, W. E., Montgomery, D. R., and Schaub, T.: The variability of root
855 cohesion as an influence on shallow landslide susceptibility in the Oregon Coast Range, *Canadian Geotechnical Journal*, 38,
856 995–1024, <https://doi.org/10.1139/cgj-38-5-995>, 2001.

857 Schuster, R. L. and Highland, L. M.: Socioeconomic and environmental impacts of landslides in the Western Hemisphere,
858 <https://doi.org/10.3133/ofr01276>, 2001.

859 Schwanghart, W. and Scherler, D.: Short Communication: TopoToolbox 2 – MATLAB-based software for topographic
860 analysis and modeling in Earth surface sciences, *Earth Surface Dynamics*, 2, 1–7, <https://doi.org/10.5194/esurf-2-1-2014>,
861 2014.

862 Sharma, A. R. and Déry, S. J.: Contribution of Atmospheric Rivers to Annual, Seasonal, and Extreme Precipitation Across
863 British Columbia and Southeastern Alaska, *J. Geophys. Res. Atmos.*, 125, <https://doi.org/10.1029/2019JD031823>, 2020.

864 Spinola, D., Margerum, A., Zhang, Y., Hesser, R., D'Amore, D., and Portes, R.: Rapid soil formation and carbon accumulation
865 along a Little Ice Age soil chronosequence in southeast Alaska, *CATENA*, 246, 108460,
866 <https://doi.org/10.1016/j.catena.2024.108460>, 2024.

867 Stock, J. and Dietrich, W. E.: Valley incision by debris flows: Evidence of a topographic signature: VALLEY INCISION BY
868 DEBRIS FLOWS, *Water Resources Research*, 39, <https://doi.org/10.1029/2001WR001057>, 2003.

869 Swanson, F. J., Benda, L. E., Duncan, S. H., Grant, G. E., Megahan, W. F., Reid, L. M., and Ziemer, R. R.: Mass failures and
870 other processes of sediment production in Pacific northwest forest landscapes, Pages 9–38, in: Ernest O. Salo and Terrance W.
871 Cundy (eds.), *Streamside Management: Forestry and Fishery Interactions*, Proceedings of a Symposium held at University of
872 Washington, 12–14 February 1986. Contribution no. 57, Institute of Forest Resources, Seattle, Washington., 1987.

873 Swanston, D. N.: Mass Wasting in Coastal Alaska, *USDA Forest Service Research Paper PNW*, 83, 1–15, 1969.

874 Swanston, D. N.: Mechanics of Avalanching in Shallow till soils of SE Alaska, *USDA Forest Service Research Paper PNW*,
875 103, 1–16, 1970.

876 Swanston, D. N.: Judging Landslide Potential in Glaciated Valleys of Southeastern Alaska, *Explorers Journal*, 214–217, 1973.

877 U.S. Forest Service: Satellite-based Change Detection Southeast Alaska,
878 <https://usfs.maps.arcgis.com/apps/webappviewer/index.html?id=12e96b1fdd1546448f8ceec6acadc372>, 2025a.

879 U.S. Forest Service: Tongass Landslide Areas: Data.gov, <https://catalog.data.gov/dataset/tongass-landslide-areas-feature-layer>, 2025b.

881 Vascik, B. A., Booth, A. M., Buma, B., and Berti, M.: Estimated Amounts and Rates of Carbon Mobilized by Landsliding in
882 Old-Growth Temperate Forests of SE Alaska, *JGR Biogeosciences*, 126, <https://doi.org/10.1029/2021JG006321>, 2021.

883 Waliser, D. and Guan, B.: Extreme winds and precipitation during landfall of atmospheric rivers, *Nature Geosci*, 10, 179–183,
884 <https://doi.org/10.1038/ngeo2894>, 2017.

885 Wendler, G., Galloway, K., and Stuefer, M.: On the climate and climate change of Sitka, Southeast Alaska, *Theor Appl
886 Climatol*, 126, 27–34, <https://doi.org/10.1007/s00704-015-1542-7>, 2016.

887 Wheeler, J. O. and McFeely, P.: Tectonic assemblage map of the Canadian Cordillera and adjacent parts of the United States
888 of America, 1991.

889 Wu, T. H., McKinnell III, W. P., and Swanston, D. N.: Strength of tree roots and landslides on Prince of Wales Island, Alaska,
890 *Can. Geotech. J.*, 16, 19–33, <https://doi.org/10.1139/t79-003>, 1979.

891 Wyllie, D. C. and Mah, C. W.: Rock Slope Engineering, 4th ed., Spon, 456 pp., 2004.

892 Zechmann, J. M., Wikstrom Jones, K. M., and Wolken, G. J.: Lidar-derived elevation data for Wrangell Island, Southeast
893 Alaska, collected July 2023, Alaska Division of Geological & Geophysical Surveys, <https://doi.org/10.14509/31098>, 2023.

894 Zechmann, J. M., Wikstrom Jones, K. M., and Wolken, G. J.: Lidar-derived elevation data for Wrangell Island, Southeast
895 Alaska, collected November 28-29, 2023, Alaska Division of Geological & Geophysical Surveys,
896 <https://doi.org/10.14509/31106>, 2024.

897

← — Formatted: Bibliography